

Iron mineral transformations and their impact on As (im)mobilization at redox interfaces in As-contaminated aquifers

Agnes Kontny¹, Magnus Schneider¹, Elisabeth Eiche¹, Emiliano Stopelli², Martyna Glodowska³, Bhasker Rathi⁴, Jörg Göttlicher⁵, James M. Byrne^{3,6}, Andreas Kappler³, Michael Berg², Duyen Vu Thi⁷, Pham T.K. Trang⁷, Pham H. Viet⁷, AdvectAs team members⁸, Thomas Neumann^{1,9}

¹ Karlsruhe Institute of Technology (KIT), Institute of Applied Geosciences, Karlsruhe, Germany

² Eawag, Swiss Federal Institute of Aquatic Science and Technology, Dübendorf, Switzerland

³ Geomicrobiology, Center for Applied Geosciences, University of Tübingen, Germany

⁴ Hydrogeology, Center for Applied Geosciences, University of Tübingen, Germany

⁵ Karlsruhe Institute of Technology (KIT), Institute for Photon Science and Synchrotron Radiation (IPS), Eggenstein-Leopoldshafen, Germany

⁶ School of Earth Sciences, University of Bristol, Bristol, UK

⁷ KLFATEFOS, Vietnam National University, Vietnam

⁸ AdvectAs members – listed in the SI 1

⁹ Technische Universität Berlin, Institute of Applied Geosciences, Berlin, Germany

For submission to *Geochimica et Cosmochimica Acta*

Corresponding author: agnes.kontny@kit.edu

This document is the accepted manuscript version of the following article:
Kontny, A., Schneider, M., Eiche, E., Stopelli, E., Glodowska, M., Rathi, B., ...
Neumann, T. (2021). Iron mineral transformations and their impact on As
(im)mobilization at redox interfaces in As-contaminated aquifers. *Geochimica et
Cosmochimica Acta*, 296, 189-209. <https://doi.org/10.1016/j.gca.2020.12.029>

This manuscript version is made available under the CC-BY-NC-ND 4.0
license <http://creativecommons.org/licenses/by-nc-nd/4.0/>

Abstract

Iron minerals are the most important arsenic host in As-contaminated deltaic sediments. Arsenic release from Fe minerals to groundwater exposes millions of people worldwide to a severe health threat. To understand the coupling of Fe mineralogy with As (im)mobilization dynamics, we analyzed the geochemistry and mineralogy of a 46 m long sediment core drilled into the redox transition zone where a high As Holocene aquifer is juxtaposed to a low As Pleistocene aquifer in the Red River delta, Vietnam. We specifically concentrated on mm- to cm-scale redox interfaces within the sandy aquifer. Various Fe phases, such as Fe- and Mn- bearing carbonates, pyrite, magnetite, hematite and Fe-hydroxides (goethite, lepidocrocite) with distinct As concentrations were identified by a combination of high-resolution microscopic, magnetic and spectroscopic methods. The concentration of As and its redox species in the different Fe-minerals were quantified by microprobe analysis and synchrotron X-ray absorption. We developed a conceptual model integrating Fe-mineral transformations and related As (im)mobilization across the redox interfaces. Accordingly, As is first mobilized via the methanogenic dissolution of Fe(III) (oxyhydr)oxide mineral coatings on sand grains when reducing groundwater from the Holocene aquifer intruded into the Pleistocene sands. This stage is followed by the formation of secondary Fe(II)-containing precipitates (mainly Fe- and Mn-bearing carbonates with relatively low As < 70 µg/g), and minor pyrite (with high As up to 5800 µg/g). Due to small-scale changing redox conditions these Fe(II) minerals dissolve again and the oxidative behavior of residual Fe(III)-phases in contact with the reducing water leads to the formation of abundant Fe(III)/Fe(II) (oxyhydr)oxides especially at the studied redox interfaces. Microcrystalline coatings and cementations of goethite, magnetite and hematite have intermediate to high As sorption capacity (As up to 270 µg/g) creating a key sorbent responsible for As (im)mobilization at interfingering redox fronts. Our observations suggest a dynamic system at the redox interfaces with coupled redox reactions of abiotic and biotic origin on a mm to cm-scale. In a final stage, further reduction creates magnetite with low As sorption capacity as important secondary Fe-mineral remaining in reduced gray Pleistocene aquifer sands while considerable Fe and As is released into the groundwater. The presented redox-dependent sequence of Fe phases at redox interfaces provides new insights of their role in As (im)mobilization in reducing aquifers of south and southeast Asia.

Over the past three decades extensive surveys have investigated the geogenic As contamination of groundwater in the densely populated regions of south and southeast Asia (e.g. Berg et al., 2001; Smedley and Kinniburgh, 2002; Ravenscroft et al., 2009; Benner and Fendorf, 2010; Winkel et al., 2011). Many studies have revealed that the mobilization of As into groundwater is related to natural processes, of which the microbially driven oxidation of organic matter coupled with the reduction of As-bearing Fe(III) (oxyhydr)oxides in the deltaic sediments is the most dominant and well-studied mechanism (Nickson et al., 2000; McArthur et al., 2001; Dowling et al., 2002; Harvey et al., 2002; Akai et al., 2004; Islam et al., 2004; Swartz et al., 2004; van Geen et al., 2013; Postma et al., 2007, 2010, 2012; Fendorf et al., 2010; Stuckey et al., 2015; Phan et al., 2019; Glodowska et al., 2020a). A characteristic feature of the As contaminated areas is that orange, often Pleistocene aquifer sands mostly show As groundwater concentrations below the WHO limit of 10 $\mu\text{g/L}$, while gray, mostly Holocene sandy aquifers have dissolved As concentrations 10 to 30 times the WHO limit (Berg et al. 2001; 2007; van Geen et al., 2013; Jung et al. 2015; Stopelli et al., 2020). Thus, color of aquifer sands, often measured as spectral reflectance, can be used as first indicator for the As status of groundwater (Horneman et al., 2004; Zheng et al. 2005; van Geen et al., 2013; Nghiem et al., 2020). The change in color indicates clear differences in the redox state of the sediments. Orange sands are mostly composed of Fe(III) (oxyhydr)oxides like ferrihydrite, goethite and hematite with Fe(II) mainly fixed in primary magnetite or silicates. To a lesser extent, gray sands still contain Fe(III) (oxyhydr)oxides but the conversion to siderite, vivianite and magnetite become important under reducing conditions. The mobility of As is closely linked to this Fe(III) to Fe(II) mineral transformation or reprecipitation (Horneman et al., 2004; Jung et al., 2015; Nghiem et al., 2020). Also, authigenic pyrite is reported as important As carrier in sediments from Bangladesh (Lowers et al., 2007). The fact that Fe mainly remains in the solid phase during transformation processes leads to a decoupling of As and Fe release into groundwater (Horneman et al., 2004; van Geen et al. 2004). Fendorf et al. (2010) even suggest that reductive transformation of ferrihydrite, as least thermodynamically stable phase, into more stable phases like goethite, hematite or magnetite enhances the immobilization of As. The transformation of ferrihydrite in presence of adsorbed As(III) and As(V) into magnetite does not necessarily lead to As mobilization, but caused incorporation of As(V) into the magnetite structure (Coker et al., 2006; Jung et al., 2015) underpinning the complexity of As (im)mobilization mechanisms in relation to Fe dynamics in natural systems.

Contrasting redox conditions in groundwater of As affected delta regions are often found adjacent to each other separated by a redox transition zone (e.g. Eiche et al., 2008; Jung et al., 2012; van Geen et al., 2013; Stopelli et al., 2020; Wallis et al., 2020) in vertical, inclined or lateral orientation. Several factors such as seasonal variations or pumping-induced changes in groundwater head and groundwater flow direction, or the type and availability of organic matter are known to influence the prevalent redox state of the aquifer (e.g. Jung et al., 2015; Stuckey et al., 2015; Eiche et al., 2017; Schaefer et al., 2017; Phan et al., 2019). Highly variable sedimentology, including fluvial channel fillings and the interfingering of marine and fluvial deposits of different grain size, can also be responsible for highly contrasting redox subsurface conditions on centimeter- to meter-scales (e.g. van Geen et al., 2013; Eiche et al., 2017).

Although many studies have investigated the mineralogy and geochemistry of As contaminated aquifer sediments with contrasting redox conditions in deltaic regions of Vietnam (e.g. Eiche et al., 2008; 2017; van Geen et al., 2013; Nghiem et al., 2020) and Bangladesh (Horneman et al., 2004; van Geen et al., 2004; Jung et al., 2012; 2015), research that explicitly considers the variable Fe mineralogy across centimeter scale redox interfaces explaining the As(III)/(V) (im)mobilization is still lacking. To tackle these knowledge gaps, our study is focused on the distribution of redox-sensitive Fe minerals and their As concentration across the interface of reduced gray to (sub)oxic orange aquifer sediments in the Red River delta, Vietnam. The well-studied field site in Van Phuc is characterized by a close juxtaposition of a high and low As aquifer (Berg et al., 2001; 2007; 2008; Eiche et al., 2008; Bostick et al., 2010; van Geen et al., 2013; Stahl et al., 2016; Rathi et al., 2017; Nghiem et al., 2019; 2020; Stopelli et al., 2020; Wallis et al., 2020).

Our aim is to understand the close interrelation between Fe mineral dissolution-precipitation and As (im)mobilization at mm- to cm-scale redox interfaces in the aquifer sand. We present geochemical and sedimentological core data and identify the Fe mineralogy from macro to micro scales by a combination of magnetic, spectroscopic and microscopic methods. For the first time, we investigated thin samples allowing us to study the role of Fe mineral textures and their intergrowth in connection with sedimentological features like small-scale grain size changes and micro flow path on the As (im)mobilization.

2. STUDY SITE

The investigated aquifer is located in Holocene to Pleistocene sediment deposits of the Red River near the village Van Phuc, approximately 15 km southeast of Hanoi, Vietnam (Fig. 1).

From earlier drilling campaigns, three distinct sediment layers (clayey silt until ~20 m depth, sand with varying amounts of silt between 20 and 50 m depth, and a gravel layer below ~50 m depth) were reported (Eiche et al., 2008; van Geen et al., 2013). The local groundwater hydrology has strongly been influenced by water withdrawals in the city of Hanoi over the last decades, which caused a reversal of groundwater flow at Van Phuc towards NW (Fig. 1c). High As and Fe concentrations in the groundwater are associated with gray, reduced sediments, while low dissolved As and Fe concentrations are present in aquifers with orange sands (van Geen et al., 2013; Stopelli et al., 2020). Intercalations of gray sand with orange sand indicate that not geological boundaries but intrusion of reduced water into the Pleistocene aquifer are responsible for a color change of the sediments (van Geen et al., 2013). Modelling of the groundwater flow for the Van Phuc area suggests average advection rates towards Hanoi of about 40 m/yr for the period from 1951 to 1971 (van Geen et al., 2013). Recent numerical model simulations by Wallis et al. (2020) illustrate that the front of the As plume migrated >1700 m over the past 60 years, starting from the river–groundwater interface to its current position. The authors concluded that the riverbed–aquifer interface constitutes a biogeochemical active hotspot that acts as the main source for elevated As concentrations. In-situ release from the Holocene sediments was largely attributed to displacement of As by phosphate from available sorption sites which explains why the As plume migrates faster compared to the reductive dissolution of Fe(III) (oxyhydr)oxides (Wallis et al., 2020). Model calculations of van Geen et al. (2013) indicate that groundwater originating from Holocene aquifer sands should have penetrated up to a distance of 2000 m into the Pleistocene aquifer sands by the year 2011 and thus contaminating the whole Holocene aquifer. In reality, a sharp decline in dissolved As concentrations can still be observed which corresponds to an As retardation factor of 16 to 20 relative to the movement of groundwater. In this context, only less than 100 m of the formerly orange Pleistocene sediment became gray, indicating that not only As but also the whole redox front has been retarded (van Geen et al., 2013). Arsenic retardation is confirmed by a hydrogeochemical study of Stopelli et al. (2020) reporting that the location of the redox transition zone (D in Fig. 1b), including a sharp decrease of dissolved As from 393 to 1.4 µg/L over a distance of only about 35 m, remained relatively stable in the studied period (2010 to 2017). The authors identified five hydrogeochemical zones (A to E) along an approximately 2 km long transect (Fig. 1b) with highly variable groundwater As, Fe and methane (CH₄) concentrations.

3. MATERIALS AND METHODS

3.1. Sampling and sample preparation

In October 2017, a sediment core (RD42: N: 20°55'18.5" E: 105°53'38.2") from about 3.3 m to 46.5 m depth was drilled with a rotating drill bit. Drill core RD42 (diameter 9 cm) is situated at ca. 1.7 km distance from the riverbank in zone D where high and low As groundwater aquifers are juxtaposed (Fig. 1, van Geen et al., 2013; Stopelli et al., 2020). The lithological characterization and description of the core, including photo documentation (example see SI 2 and Fig. 3), took place in the field directly after the drilled core segments were opened and split into halves using a ceramic knife. The core description followed the protocol of the International Continental Drilling Program (ICDP) and involved color (Munsell soil color charts), grain size and high-resolution measurements of magnetic susceptibility. Our investigation focused on the Fe minerals in the redox transition zone of the sandy aquifer between 19.5 and 41.9 m depth.

Different types of subsamples, taken from the central part of the core to minimize contamination with the drilling fluid (see hole in Fig. 3d), were collected directly in the field: a) N₂-flushed bulk samples for determination of mineralogy, geochemistry and magnetic susceptibility (n=74), b) unflushed bulk samples for grain size analysis (n=78), and c) undisturbed N₂-flushed stitch samples for thin section analysis (n=22). The samples flushed immediately with nitrogen gas N₂ after sampling were cooled with ice packs in a cooling box during transport back to Germany to minimize microbial activity. This procedure allowed keeping samples roughly around room temperature. Water- and air-tight zip log bags (PET/PE-LD/Aluminum stand-up pouches LamiZip bags (DAKLAPACK) with high barrier properties against oxygen and water vapor and protection against UV radiation were used to minimize sample alteration.

Bulk samples for geochemical analysis were oven dried for 48 h at 40°C and ground to a homogenous fine powder using a ball mill or disc mill (both made of agate), depending on sample quantity. Bulk samples for mineralogical analysis were dried in a desiccator with drying granulate under N₂ atmosphere at 40°C for 48 h to avoid alteration of redox sensitive phases.

To preserve the original sediment texture and redox state during sampling, transport and preparation, stitch molds (35 mm in diameter and 55 mm in length or 30 x 50 mm in size, see Fig. 3d) were used to enable spatially resolved geochemical and microscopic analysis. The final size of the thin sections was 28 x 48 mm. After storage and transport under N₂ atmosphere, the sediment in the stitch forms was dried in a desiccator with drying granulate under N₂ atmosphere at 40°C. Afterwards, the samples were impregnated with a synthetic resin (Araldite 2020). This resin was chosen because its high viscosity at low temperatures allowed

impregnation at temperatures below 40°C. The subsequent hardening process was conducted under vacuum to ensure in-depth impregnation and exclusion of oxygen. After splitting the massive blocks, one side was used to produce a classical thin section for microscopy and the mirror side for spatially resolved synchrotron analysis (μ -XANES).

3.2. Methods and analysis

Grain size distribution of 78 sediment samples was determined by a combination of sieving ($>63\ \mu\text{m}$) and laser granulometry ($<63\ \mu\text{m}$) with CILAS PSA 1064 at the “Materials Testing and Research Institute” (MPA) at KIT.

Trace element concentrations of grounded sample material ($n=74$) was analyzed using energy dispersive X-ray fluorescence analysis (ED XRF) (Epsilon 5, PANalytical). The detection limit for arsenic was $\sim 1\ \mu\text{g/g}$. Wavelength dispersive XRF (WD XRF) (S4 Explorer, Bruker) of fused beads was used to determine the major element geochemistry of the same samples. Total carbon (TC), total organic carbon (TOC) and total sulphur (TS) contents were determined with a carbon sulfur analyser (CSA CS-2000, ELTRA) ($n=74$). Total inorganic carbon (TIC) was calculated as the difference between TC and TOC ($n=25$).

Bulk mineral composition ($n = 74$) including semi quantitative evaluation of major and minor phases was determined by X-ray diffraction (XRD) (Bruker D8 Discover). $\text{CuK}\alpha$ -radiation was used and the samples were scanned from 2° to $82^\circ\ 2\theta$ with an increment of $0.02^\circ\ 2\theta$ at 0.4 sec. The relative mineral abundances were estimated from integrated peak areas using the HighScore-Plus software from Malvern PANalytical GmbH and the Inorganic Crystal Structure Database (ICSD) for phase identification.

Volume magnetic susceptibility was measured in the field ($n=349$) with a handheld SM-30 Kappameter (ZH Instruments) in 10 cm intervals along the halved cores in order to detect the Fe mineral distribution. Additionally, temperature dependent magnetic susceptibility in the temperature interval -192°C (liquid nitrogen temperature) to 710°C was determined on 46 N_2 flushed bulk samples from the sandy aquifer with a KLY-4S Kappabridge (Agico) for magnetic Fe mineral identification. High temperature measurements (room temperature to 710°C) were measured in an inert argon atmosphere to minimize oxidation.

Microscopic investigations on 27 thin sections from 22 depths were carried out to identify the mineralogy with a special focus on Fe minerals. Optical light microscopy was used to describe micromorphology and sediment properties. To retrieve mineral chemical information scanning electron microscopy (SEM) coupled to energy dispersive spectroscopy (EDS) was done using

a Tescan Vega 2 SEM at an accelerating voltage of 15 kV and a working distance of 15 mm, using the secondary electron and backscatter signal. Thin sections were mounted on specific 3D-printed sample holders and sputtered with a carbon or gold thin film coating. Identification of elements in spot analyses and their distribution using the mapping option of automatic or manual search of elements were performed using the analytical software SwiftED (version 1.2). Element abundances were determined from the EDS spectra by integrating peak areas and normalizing the results to 100%. Some of the thin sections were analyzed at the Laboratory for Electron Microscopy at KIT with a FEI Quanta 650 FEG ESEM to obtain a higher resolution. Electron probe microanalysis (EPMA) of three thin sections from 22 m, 30 m, and 41 m depth was done at „Zentraleinrichtung Elektronenmikroskopie“ (ZELMI) at the TU Berlin with a JEOL JXA-8530F. Mineral chemical data were obtained at 15.0 kV by an EDX system with silicon drift detector that is coupled to the EPMA. The detection limit of As was around 70 µg/g.

Four samples (20 m, 21 m, 30 m, 37 m) were analyzed with ^{57}Fe Mössbauer spectroscopy, which is sensitive for short-range interactions in Fe minerals and allows for their identification. Dried samples were loaded in plexiglas holders (diameter 1 cm²) and stored under N₂ atmosphere prior to loading inside a closed-cycle exchange gas cryostat (Janis cryogenics). Measurements were collected at 77 K with a constant acceleration drive system (WissEL) in transmission mode with a $^{57}\text{Co}/\text{Rh}$ source and calibrated against a 7 µm thick α - ^{57}Fe foil measured at room temperature. Mössbauer hyperfine parameters, which is the collective name given to the parameters that characterize a typical Mössbauer spectrum when fitted, were center shift (CS), quadrupole splitting (QS), which is also referred to as the quadrupole shift in the case of six-line spectral components ($\text{Qshift} = 0.5 \cdot \text{QS}$), and hyperfine magnetic field (H). The mathematical function used for the fitting of all spectra was a Voigt Based Fitting (VBF) routine (Rancourt et al., 1991) implemented in the software Recoil (University of Ottawa). Combined, these parameters are used for determination of oxidation state and phase identification. Furthermore, the areas under each phase are then used to estimate a relative contribution of each phase to the composition of Fe in the sample. The half width at half maximum (HWHM) was fixed to a value of 0.130 mm/s for all samples.

Focused X-ray absorption spectra (µ-XAS) were collected on µm-scale at the SUL-X beamline of the Institute for Photon Science and Synchrotron Radiation (IPS) at KIT. The X-ray absorption near edge structure (µ-XANES) spectra was measured at the Fe (7,112 eV, calibrated by metal foil) and As (11,919 eV, calibrated by gold foil) K-edges at room temperature using a Double Crystal Monochromator (DCM Si111). The spot size was 40 µm

(horizontal) x 30 μ m (vertical). Data were processed with the Athena software (Ravel and Newville, 2005). Subsequent linear combination fitting (LCF) using the Athena software revealed the Fe mineral composition and As(III):As(V) ratio for 21 spot measurements in the thin section from 41 m depth.

4. RESULTS

4.1 Lithology, magnetic properties and geochemistry of aquitard and aquifer deposits

The sediment core RD42 was drilled into the redox transition zone D (Fig. 1), intercepting a top (3-19.5 m) and bottom (42-46.5 m) silt-clay aquitard with a sandy aquifer intercalated between 19.5 and 42 m and a gravel aquifer > 46.5 m (Fig. 2). Based on the color and thus the inferred redox state of the sediment, the sandy aquifer can be separated into an upper gray, reduced sand dominating between 20 and 30 m, and a yellow-brown, less reduced sand between 30 and 42 m. No typical uncontaminated orange sand was drilled. In both of these sections, and especially at their top and bottom boundaries, localized redox interfaces in the cm scale were identified, manifested in color and magnetic susceptibility differences (orange bars in Fig. 2). Apart from the color, the two contrasting sand layers in the aquifer were characterized by different hydrogeochemical characteristics with high dissolved As concentrations especially in the upper part between 22 and 25 m depth (Stopelli et al., 2020).

The **top aquitard** was mainly composed of silty material was drilled.(57-88 wt%) with substantial variations in the clay (4-28 wt%) and sand (0-34 wt %) content (average values see Table 1). Two distinct clay-rich layers at 6.5-8 m and 12-16 m with a beige color, contrasted significantly from the predominantly dark gray to black, organic rich silt layers. Thin sandy layers, which were less than 1 cm thick, were identified throughout the whole aquitard. From 16.5 to 21,0 m depth, the sand content increased gradually from below 10 to above 70 wt%. Along this silt-sand transition zone, clay rich layers and Fe concretions were observed.

The **bottom aquitard** extended from 42,0 to 46.5 m depth and consisted of homogeneous brown material with an average silt content of 79 wt%, 16 wt% clay and 5 wt% sand. Below 46.5 m depth a coarse-grained gravel aquifer occurred with unknown extent.

The **sandy aquifer** reached from 19.5 to 42.0 m depth and consisted of 14-89 wt% sand, of 10-77 wt% silt and of 1-9 wt% clay (average values see Table 1) with four prominent silty intercalations at 23 m, 27 m, 30 m and 34 m depth with 65 wt% silt, 7 wt% clay and 28 wt% sand, on average. Numerous mm to cm thick clay dominated layers as well as some thinner

layers with isolated clayey concretions were periodically intercalated throughout the entire aquifer. The color of the sand in the aquifer was mainly yellow-brown between 20 and 22 m and below 30 m depth (see Fig. 3 and SI2), which is slightly different to the typical color described for the suboxic Pleistocene fluvio-deltaic sand deposits (e.g. Eiche et al., 2008; van Geen et al., 2013). Between 22 and 30 m, gray colored sands occurred, clearly indicating a more reduced state. Within the gray colored sandy section, orange-brown and yellow-brown intercalations, sometimes with a higher clay and silt content were observed (SI3). The different colors in this depth interval indicated an intercalation of moderately and highly reduced sediments, which were mainly related to differences in grain size and thus, probably permeability. A narrow gray sand layer also occurred at the bottom of the less reduced, yellow-brown sand directly above the bottom aquitard at about 41 m depth (Fig. 2, 3d, SI3). Redox interfaces with rusty-orange color were present as small-scale centimeter to decimeter transitions within and between yellow-brown and gray sands (see orange bars in Fig. 2). These interfaces were always characterized by strong color / redox gradients (Fig. 3) and were the focus of the detailed mineralogical investigations in the following chapters.

High-resolution magnetic susceptibility (k) (Fig. 2) reflects the type and amount of magnetic minerals in the sediment, and therefore is lithology sensitive (e.g. Horneman et al., 2004). In principle, k indicates the Fe concentration and whether the Fe is present in paramagnetic or ferromagnetic minerals (Tarling and Hrouda, 1993). Aquitard and aquifer sediments from the investigated drill core exhibited different k pattern (Fig. 2). The upper aquitard clayey silts showed a tendency to higher k average values than aquifer sand. In the top aquitard, the beige coloured clay intercalation had about three times lower values ($88 \pm 62 \times 10^{-6}$ SI) than the dark, organic-rich sediments ($359 \pm 224 \times 10^{-6}$ SI). The bottom aquitard showed average k values of $144 \pm 45 \times 10^{-6}$ SI, which is lower than in the dark coloured top aquitard (Table 2).

The yellow-brown sands displayed k values between 29 and 413×10^{-6} SI ($97 \pm 76 \times 10^{-6}$ SI on average), which is much less variable and distinctly lower than for the gray sands with values ranging between 26 and 2900×10^{-6} SI ($198 \pm 368 \times 10^{-6}$ SI on average). Distinct layers and peaks with k values above 500×10^{-6} SI in the gray sand indicated a clear contribution of ferrimagnetic Fe minerals (Tarling and Hrouda 1993).

In addition to magnetic susceptibility, Fig. 2 shows the distribution of Fe_2O_3 , As, MnO, total sulfur (TS), total carbon (TC, dominated by organic carbon) and P_2O_5 contents along the sediment core (see also SI3). Fe_2O_3 , P_2O_5 and As are clearly enriched in the top and bottom aquitard especially compared to the yellow-brown and gray sands (Table 1). The As concentration in the top aquitard is relatively high, with an average of $13.8 \mu\text{g/g}$ (max $30 \mu\text{g/g}$),

and nearly double of the bottom aquitard. Concentrations of Fe_2O_3 , As, TS and TC decreased in the lower part of the top aquitard. The geochemical character and color likely indicate a different depositional environment (Eiche et al., 2008; 2017; van Geen et al., 2013). Gray sands from the aquifer showed lower As (2.3 $\mu\text{g/g}$ on average) and Fe_2O_3 (1.5 wt% on average) compared to the yellow-brown sand (As: 4.6 $\mu\text{g/g}$, Fe_2O_3 : 2.5 wt%). Total C in the yellow-brown sand was about twice as high, on average, as in the gray sand (Table 1).

Redox interfaces reveal a particular different composition compared to yellow-brown and gray sands with three times higher Fe_2O_3 , nearly four times higher As and five times the TC concentrations compared to gray sands (Fig. 2 and data given in SI3). The aquitard-aquifer transition at 19.5 m depth is characterized by relatively high Fe_2O_3 and As concentrations of 11 wt% and 16.5 $\mu\text{g/g}$, respectively (Fig. 2). Total S and TC showed peaks in the sandy redox interfaces at 22 and 30 m depth. High MnO concentrations were found at 20.7 m depth. These redox interfaces with geochemical gradients suggest that the aquifer from the redox transition zone (zone D in Fig. 1) is geochemically highly reactive.

4.2. Iron minerals in the aquifer sand

Identification and characterization of accessory Fe phases is demanding because of their trace amount, heterogeneous distribution, small grain sizes, and sometimes low crystallinity. Often, they only can be identified indirectly (e.g. Horneman et al., 2004; Eiche et al., 2008). Table 2 summarizes the Fe minerals in the aquifer sand, which were recognized by bulk and space-resolved methods in the investigated core. The most important Fe minerals identified in the yellow-brown sands were goethite, ilmenite, hematite and magnetite (Table 2). Microscopic investigations have shown that ilmenite and rarely magnetite were found as detrital grains, while goethite and hematite formed coatings around detrital quartz and feldspar grains. Iron-bearing carbonates (siderite, ankerite) and ferrihydrite were identified in the yellow-brown sands and at the redox interfaces. The most important Fe mineral in the gray sand was magnetite. In addition to Fe(III) (oxyhydr)oxides and Fe-(Mn-)-bearing carbonates, some of the redox interfaces are characterized by Fe sulfides (pyrite; only at 22 and 30 m) and secondary Fe-bearing phyllosilicates. Evidence for ferrihydrite from Mössbauer spectra and thermomagnetic data were not explicit clear, but Nghiem et al. (2020) described it as important Fe(III) phase using X-ray absorption spectroscopy in the study area.

4.2.1. Magnetic susceptibility

Temperature dependent magnetic susceptibility ($n=46$) was used to specifically identify ferrimagnetic Fe-bearing minerals and their depth distribution in the sand aquifer. Magnetite (Fig. 4a) was identified as the most important ferrimagnetic mineral by the Verwey transition (T_V) at around -150°C , which indicates a monoclinic to cubic first order structural transition, and the Curie temperature at around 580°C (Dunlop and Özdemir, 1997). A significant dominance of magnetite was observed in the gray sand in accordance with magnetic susceptibility peaks and higher k average values measured along the sediment core in the aquifer (Fig. 2), and in line with more reducing conditions. In the yellow-brown sand, T_V , which is sensitive for the detection of very small amounts of magnetite, was only rarely observed. At the redox interfaces, magnetite occurred as minor magnetic phase beside siderite (Fig. 4b) and lepidocrocite (Fig. 4c). All phases occur together in different amounts in one sample (Fig. 4d). Siderite and lepidocrocite were identified by their characteristic transition temperatures. The transformation of Fe (oxyhydr)oxides like lepidocrocite into magnetite is a common feature in temperature dependent magnetic susceptibility measurements, and it can be facilitated by organic matter in the sample (e.g. Till and Nowaczyk, 2018). Through comparison with measurements of pure minerals (Fig. 4e, f), the transition T_{t1} is interpreted to indicate lepidocrocite, which partially transforms further into a ferrimagnetic phase such as maghemite or magnetite above about 280°C . This interpretation explains the irreversibility of the heating and cooling phase. Lepidocrocite was mainly observed in the upper part of the sand aquifer but vanished in the gray sand (compare T_{t1} in Fig. 4b with Fig. 4d). Instead, Fe-bearing carbonates (T_{t2} in Fig. 4b and d) and magnetite (Fig. 4a) dominate. Iron-bearing carbonates also show a transformation to magnetite, but at about 380°C (Fig. 4f).

The low temperature curves (Fig. 4b, d) show a strong drop in k below -190°C indicative of goethite (Guyodo et al., 2003) or ferrihydrite (Berquo et al., 2007; Liu et al., 2008). This signal has been observed in most samples which are not dominated by magnetite, addressing the importance of these Fe (oxyhydr)oxides.

4.2.2. Mössbauer spectroscopy

Mössbauer hyperfine parameters at 77 K (-196°C) were measured for four samples (location see Fig. 2) in order to confirm and complement the information on Fe-bearing minerals retrieved from temperature-dependent magnetic susceptibility measurements (Fig 5a). In all samples, a well-defined sextet, which is likely ordered goethite ($\alpha\text{-FeOOH}$) (e.g. Cornell & Schwertmann, 2003) was observed. A clear paramagnetic narrow doublet was also observed

with hyperfine parameters most closely associated with an Fe(III) phase. This doublet likely corresponds to a combination of short range ordered phases like lepidocrocite (γ -FeOOH) or ferrihydrite ($\text{Fe}^{3+}_{10}\text{O}_{14}(\text{OH})_2$) (e.g. Li et al., 2011), possibly in addition to Fe(III) in another phase such as a Fe-bearing phyllosilicate. The quadrupole fitting of 0.63 mm/s was lower than typical of ferrihydrite and tends more towards values associated with lepidocrocite, which agrees with the thermomagnetic curve at 19.7 m depth shown in Fig. 4c. However, thermomagnetic investigations further showed a significant decrease of lepidocrocite with depth in the upper part of the sand aquifer. This observation suggests that ferrihydrite could also be widespread as an Fe (oxyhydr)oxide in the sand aquifer. The 77 K measurements also revealed the presence of a relatively minor wide doublet corresponding to Fe(II), which based on hyperfine parameters we speculate to correspond to Fe in a Fe-bearing phyllosilicate or potentially even green rust (fitting parameters and relative abundancies are given in SI 5). At 30.0 and 36.4 m depth, Mössbauer spectra indicated some hematite (Fig. 5). In order to gain additional information, Mössbauer spectra at 5 K (-268 °C) were collected for three samples (Fig. 5b). The paramagnetic Fe(III) doublet, as observed at 77 K remained, though with lower relative abundance as compared to the other sextets and Fe(II) site. This suggests that some of the Fe(III) underwent magnetic ordering at a temperature below 77 K, i.e. below its magnetic blocking temperature. Such behavior is typical of short range ordered phases such as lepidocrocite or ferrihydrite and confirms the interpretation of the magnetic measurements that the strong increase of magnetic susceptibility below 70 K (-190°C) is related to these Fe(III) (oxyhydr)oxides. The remaining Fe(III) grey doublet at 5 K likely belongs to a phase which does not undergo magnetic ordering and we interpret to be a Fe-bearing phyllosilicate (e.g. chlorite).

4.3. Spatially resolved Fe mineralogy at redox interfaces

Microscopy combined with EPMA, SEM and μ XANES provide spatially resolved information on texture, intergrowth and composition of the Fe-bearing minerals and their As concentration and speciation will be shown for the redox interfaces at 20 m, 30 m and 40 m (Fig. 2). Microscopy allowed us to differentiate between detrital grains (ilmenite and magnetite) and secondary minerals and their transformations formed after the deposition of the sediments. At the redox interfaces, these secondary minerals were Fe-bearing carbonates and cementations composed of Fe carbonates, Fe phyllosilicates, Fe (oxyhydr)oxides (goethite, magnetite, hematite), and pyrite framboids (Table 2).

4.3.1 Iron carbonates

Iron-rich carbonates were frequent in the sandy matrix of the redox interfaces where they occurred disseminated compared to other Fe precipitates. Three different texture types were distinguished: spherical and irregular shaped grains with alteration rims (Fig. 6a), cementation networks (Fig. 6b), and pure siderite overgrowth with skeletal crystal growth (Fig. 6c). All three texture types occurred within close distance in the same thin section. The grains were 20-100 μm in size and mostly grown as single grains in pores or as overgrowth of transported, primary minerals. Some grains also showed lobate grain boundaries indicating dissolution (Fig. 7). The carbonate grains and the cementation networks displayed clear signs of decomposition into clay minerals and Fe (oxyhydr)oxides at the rims (Fig. 6a), which is confirmed by the Al and Fe distribution shown in the elemental mapping images in Fig. 7. EPMA revealed that the carbonate grains were Fe rich (47-76 wt% Fe_2O_3) with 2-11 wt% CaO and 0.6-6.4 wt% MnO. Iron-rich carbonates explain very well the increase in magnetic susceptibility above 380 °C in the temperature dependent magnetic susceptibility (Fig. 4b, d). Arsenic concentrations were low in the grain centers (near the detection limit of 70 $\mu\text{g/g}$ for the electron microprobe) and reached values of around 140 $\mu\text{g/g}$ in the altered rim suggesting that Fe carbonate alteration can be an important mechanism for As immobilization. These Fe-carbonate cementations with As concentration distinctly above the detection limit of the electron microprobe only occurred along redox interfaces. Pure siderite cementations with skeletal crystal growth (Fig. 6c) were observed throughout the sandy aquifer and showed As concentrations, which were always below the detection limit of the electron microprobe (< 70 $\mu\text{g/g}$).

4.3.2. Iron (oxyhydr)oxides

At redox interfaces, we also observed gel-like precipitates and small-scale intergrowth of different Fe(II/III) and Fe(III) minerals. These microcrystalline Fe precipitates occurred in two different morphologies, both as coatings around primary grains such as quartz, feldspar and phyllosilicates (Fig. 8a-d) and as massive cementations in the pore space (Fig. 9). Spatially resolved μXANES revealed that these Fe precipitates consisted of goethite, magnetite and hematite (Fig. 10d). These were the Fe (oxyhydr)oxides that caused the rusty-orange color and cluster-like appearance in the redox interface shown in the thin section of Fig. 3e. The coatings were tens of μm thick. In their inner part, they were dominantly composed of magnetite and hematite (white color in SEM images of Fig. 8b-d and Fig. 9c) whereas the sponge-like rims are dominated by goethite (gray color in SEM images of Fig. 8b-d and Fig. 9c).

In these coatings, EPMA revealed a low As concentration ($<70 \mu\text{g/g}$) in magnetite/hematite, while the As concentration in goethite is distinctly higher ($270 \mu\text{g/g}$; Fig. 8c). The sponge-like goethite-rich outer rims (Fig. 8d) resemble Fe precipitates in microbial mats or cell surfaces with aggregation of nano- to microcrystals (e.g. Voegelin et al., 2013; Sanchez-Roman et al., 2014). Therefore microbial-mediated formation seems to be likely for these Fe precipitates. Cementations composed of these Fe (oxyhydr)oxides also occurred as concentric rings or layers with periodic precipitation of microcrystalline magnetite/hematite and goethite (Fig. 9). Such structures are known e.g. from sediments as Liesegang bands with characteristic supersaturation of ions in a solution, followed by nucleation and depletion (Sultan and Abdel-Rhman, 2013). These Fe precipitates showed As concentrations of up to $480 \mu\text{g/g}$ in the goethite-rich areas and up to $300 \mu\text{g/g}$ in the magnetite/hematite-rich areas (Fig. 9c) indicating sorption and incorporation of As. In addition, EPMA showed that these Fe precipitates (Fe_2O_3 : 87.17wt%) contained low concentrations of SiO_2 (2.9 wt%), Al_2O_3 (2.8 wt%), CaO (0.28 wt%) and SO_3 (0.20 wt%) and a remarkably high P_2O_5 concentration of 4.3 wt%, which could be an indication for an origin from oxidation of Fe(II) in groundwater (e.g. Voegelin et al., 2010). Elemental mapping for these elements are shown in Fig. 9 (lower row).

4.3.3. Arsenic speciation in Fe (oxyhydr)oxide precipitates

We measured spatially resolved μXANES at the Fe and As K-edge of the Fe precipitate coatings and cementations. These measurements revealed that As(III) and As(V) species occurred in the Fe (oxyhydr)oxides, but with a different ratio (Fig. 10). In the coatings with a higher goethite:hematite + magnetite ratio (80:12 + 8), the As(III):As(V) ratio is 71:29 ($n = 15$). In the central areas of the cementations, the As(III) content decreased while As(V) was increasing (53:47, $n=6$). The cementations were also characterized by a lower goethite (70%) and higher hematite + magnetite content (20 % + 10%). The decrease in As(III) and increase in As(V) suggest that the central parts of cementations, which are assumed to be older, were formed in a less reducing environment compared to more reducing conditions where the presumably younger coatings precipitated. The older massy cementations had more time to interact with the groundwater and the more mobile As(III) can be preferentially released or oxidized leading to a more balanced As species ratio. It also has to be mentioned that the redox transformation of As (III) may be strongly influenced by electron transfer among Fe(III) and Fe(II) or S(-II). During this electron transfer, As(III) can be oxidized to As(V) in reducing environment (e.g. Oscarson et al., 1980; Huang et al., 1982; Phan et al., 2019). This process can be purely abiotic through Fe (III) phases or biotic through microbial activity.

4.3.4. Pyrite

Pyrite framboids were locally observed at the redox interfaces at 22 and 30 m depth concurrent with increased TS (0.019 wt%) and TC (0.32 and 0.39 wt%) concentrations in adjacent silty layers. At both depths, pyrite formed framboids with different crystal shapes of about 5 to 20 μm in diameter, composed of octahedral or cubic microcrystals of a size of about 0.5-1 μm (Fig. 11a, b). Aging of the pyrite framboids changed their shapes towards euhedral pyrite aggregations with slight zonation (Fig. 11c). Commonly, framboids form chains or clusters along fluid pathways of higher permeability compared to the nearby microenvironment (Fig. 11d). The observed framboidal shape is typical for biogenic pyrite formation coupled to sulphate reduction (e.g. Sawlowicz, 1993; Wilkin et al., 1996). Some pyrite aggregates showed lobed surfaces and cracks indicating dissolution. The EPMA revealed only slightly varying Fe:S atomic ratios (33:67 to 37:63 for $n=27$) clearly indicating pyrite stoichiometry rather than mackinawite or greigite, which are assumed to be precursor phases of pyrite (e.g. Wilkin et al., 1996). Arsenic concentrations in pyrite varied from below detection limit of the electron microprobe (70 $\mu\text{g/g}$) to 5800 $\mu\text{g/g}$. Fresh framboids contained higher As concentrations (Fig. 11b) than altered pyrite crystals (Fig. 11c). Similar As concentration in pyrite have been described from Bengal Basin sediments in Bangladesh (1500 -3200 $\mu\text{g/g}$; Lowers et al., 2007).

5. DISCUSSION

5.1 The role of redox interfaces in the redox transition zone

Previous studies have shown that groundwater high in As was advected from the Holocene aquifer into the low As Pleistocene aquifer at the study site at Van Phuc due to the increased groundwater abstraction in Hanoi (Berg et al., 2008; van Geen, 2013; Wallis et al., 2020). As a consequence, the groundwater moves from the river bank in the SE towards NW through different hydrogeochemical zones (A to E; see Fig. 1). These zones are characterized by distinct As mobilization and retardation processes, ultimately affecting groundwater As and Fe concentration (Stopelli et al., 2020). Our focus was the redox transition zone D in the Van Phuc transect (Fig. 1), which is characterized by changing redox conditions indicated by gray to yellow-brown sands (SI 2, SI3 and Fig. 2) with a variety of biotic and abiotic processes that contribute to As (im)mobilization (Glodowska et al., 2020b, c). The dominance of gray sand in the upper part of the sand aquifer is linked to high dissolved As ($>200 \mu\text{g/L}$), Fe^{2+} and CH_4 concentrations between 22 and 25 m indicating methanogenic conditions (Stopelli et al., 2020).

Dissolved organic carbon input is related either to the aquitard clays above the sand aquifer (e.g. Stopelli et al., 2020), or the transport from the interface of the Red River (Wallis et al., 2020). This dissolved carbon source can be used by microbes in the sand aquifer for fermentation and methanogenesis and thus, induce Fe(III) and sulfate reducing conditions leading to a reductive dissolution of Fe(III) bearing minerals and a concurrent release of S^{2-} , PO_4^{3-} , HCO_3^- , Fe^{2+} and As (Glodowska et al., 2020b). The redox interfaces investigated in our study occur mainly near the boundaries to the top and bottom aquitard and between gray and yellow-brown aquifer sands, but they are also ubiquitous within the aquifer where grain sizes varied significantly. The occurrence of redox interfaces along hydraulic barriers suggests that their formation is flow-controlled and local supersaturation is responsible for the formation of the Fe(II) and Fe(III) phases in these microenvironments where mineral dissolution and re-precipitation are coupled in spatially confined areas. We suggest that Fe mineral precipitation-dissolution and transformation at these redox interfaces play an important role in As (im)mobilization dynamics.

5.2 Microscale Fe mineral transformations at the redox interfaces

This study clearly shows that micro-scale dissolution-precipitation and transformation reactions are significant processes with regard to As (im)mobilization. Our study suggests a highly dynamic setting at redox interfaces where Fe minerals like pyrite and Fe-bearing carbonates can be dissolved again, or transformed into Fe (oxyhydr)oxides indicating closely coupled redox processes. Figure 12 shows a conceptual model integrating known mechanisms (e.g. Horneman et al., 2004; Lowers et al., 2007; van Geen et al., 2013) with the results of this study.

Iron and Mn carbonates: The onset of reducing conditions initiates the dissolution of the primary coatings and the release of As and Fe into the groundwater. We suggest that the frequent presence of Fe- and Mn-bearing carbonates at the redox interfaces according to $Me^{2+} + HCO_3^- \rightarrow MeCO_3 + H^+$, ($Me = Ca^{2+}$, Fe^{2+} or Mn^{2+}) is either the result of anaerobic methane oxidation (Beal et al., 2009; Zhu and Dittrich, 2016; Aromokeye et al., 2020), or of microorganism-mediated CH_4 oxidation of fermented organic matter coupled with Fe(III) and Mn(IV) reduction (Glodowska et al., 2020c). The anaerobic oxidation of methane coupled to Mn(IV) and Fe(III) reduction is described as a globally important methane sink, even in the absence of sulfate (e.g. Beal et al., 2009). Methane derived ^{13}C -depleted carbonate formation associated with rhodocrosite ($MnCO_3$) has been described e.g. for sediments of the Franciscan complex in the USA (Hein and Koski, 1987), which supports our interpretation of neoformation of carbonates associated with CH_4 oxidation (Fig. 12).

Microcosm batch experiments using in-situ organic matter and sandy sediments from one of the here investigated redox interfaces at 30 m depth proved that Fe(III) reduction indeed took place, but only a small amount of the Fe^{2+} was actually released to solution while the majority of Fe(II) remained in the solid phase (Glodowska et al., 2020a). These results fit very well to our observation of an *in-situ* formation of Fe (and Mn) carbonates within the sand at the redox interfaces. The observed carbonates are mainly not pure but mixed Fe-, Mn- and Ca-bearing carbonates (Fig. 7). The center of the carbonate is dominated by Mn and Ca, whereas the rims become richer in Fe. This shows that initially Mn(IV)-reducing conditions similar to the uncontaminated Pleistocene aquifer with orange sands (Eiche et al., 2008) were prevalent. In the further course of reducing groundwater intrusion and likely the increase in CH_4 concentration, the Fe dominated rims (Fig. 7) and skeletal siderite (Fig. 6c) are formed throughout the sandy aquifer.

Another possible process that can explain the presence of mixed carbonates within the redox interfaces is the oxidation of Fe^{2+} , which intruded with the reduced front, coupled with MnO_2 reduction. The released Mn^{2+} can precipitate as carbonate together with some of the remaining Fe^{2+} and with Ca^{2+} . Elevated concentration of dissolved Ca^{2+} , Mn^{2+} and Fe^{2+} are reported from an upstream well close to the redox transition zone (Stopelli et al., 2020) supporting the idea of multiple coupled redox and precipitation-dissolution processes.

Iron (oxyhydr)oxides composed of microcrystalline goethite, hematite and magnetite are the dominant Fe-phases within the redox interfaces (Fig. 12). Very fine layered alternating Fe (oxyhydr)oxides (Fig. 8b-d, 9b-c) suggest recent formation due to coupled biogeochemical processes. Oxidation of aqueous Fe^{2+} is known to form amorphous to short-range ordered nanoscale Fe(III)-precipitates (Voegelin et al., 2010, 2013, 2019; Schaefer et al., 2017; Senn et al., 2018). Due to their large specific surface area and thus high sorption capacity, these Fe(III)-precipitates are highly efficient in retaining As oxyanions and phosphate (Mayer and Jarrell, 2000; Roberts et al., 2004). However, their microcrystalline nature makes them highly susceptible to redox changes and increases their dissolution kinetics (Voegelin et al., 2013).

The occurrence of crystalline Fe (oxyhydr)oxides is in agreement with calculated mineral saturation indices in Van Phuc groundwater by Stopelli et al. (2020) who postulated a potential depletion of short range ordered Fe(III) phases like ferrihydrite, and the occurrence of more crystalline phases like goethite and hematite. A possible transformation of ferrihydrite into goethite, lepidocrocite and magnetite can take place in reducing environments as a result of a reaction between dissolved Fe^{2+} and ferrihydrite (Hansel et al. 2005). Crystallization increases with time and the solid phase obtained depends also on temperature and pH. Low and high

values of pH (2-5 and 10-14) favor the formation of goethite, while hematite is preferred at neutral pH (Cudennec and Lecerf, 2006). In zone D the pH is near neutral (Stopelli et al., 2020) and other causes than pH variations must be considered for the cyclic precipitation of the Fe (oxyhydr)oxides. When carbonate is added to a system, the reactive surface area of goethite is altered and agglomeration even enhanced (Chen et al., 2020). Li et al. (2011) showed that poorly crystalline ferrihydrite can also be reductively transformed by dissimilatory Fe(III)-reducing bacteria to magnetite indicating a microbial influence on the nanocrystalline magnetite formation. This is a reasonable explanation for the widespread occurrence of magnetite especially in the gray aquifer sands (Fig. 12), and the subordinate occurrence of ferrihydrite (Table 2). A microbially assisted ferrihydrite transformation is also in agreement with observations from batch experiments using the same sediments from Van Phuc, where Fe(III)-reducing conditions only resulted in very little Fe^{2+} release indicating the importance of Fe(III) mineral transformation within the sediment (Glodowska et al., 2020a).

Spatially resolved μXANES spectroscopy revealed that small-scale goethite-rich areas exist next to magnetite-/hematite-rich areas (Fig. 8, 10), confirming the relevance of oscillating redox changes that are often spatially confined. According to Hansel et al. (2005), magnetite is preferentially formed at the expense of goethite or lepidocrocite. This process occurs when surface loadings of ferrihydrite with Fe^{2+} are high (1.0 mmol Fe^{2+}/g), suggesting high rates of Fe(III) reduction. The strongest reducing conditions in our aquifer were found in the gray sand between 20 and 30 m depth, which is documented by high CH_4 and NH_4^+ concentrations in the groundwater (Stopelli et al. 2020), and the abundance of magnetite, which is suggested by higher magnetic susceptibility (Fig. 2, 3). Therefore, magnetite formation, either through abiotic or biotic formation mechanisms, is suggested to indicate a final stage in the Fe (oxyhydr)oxide transformation (Fig. 12).

Iron sulfides: Microbially mediated sulfate reduction has been suggested as important sink for dissolved As in the Van Phuc transect by a microbial community analysis and hydrogeochemical study of Glodowska et al. (2020b). Sulfate reduction coupled with Fe sulfide mineral precipitation is reported to occur at the riverbank and in the orange to beige-brown Pleistocene sands (Wallis et al., 2020). We found pyrite framboids, a typical microbial mineralization product, at the top (22 m) and bottom (30 m) redox interfaces of the gray aquifer sand. These two zones are characterized by the transition from yellow-brown to gray sand (Fig. 2). Pyrite has formed as a result of microbial sulfate reduction either in contact with silty intercalations due to residual S content, or due to the sulfate dissolved in the Pleistocene

groundwater (Eiche et al., 2008). At some places, we observed chains of pyrite framboids along pore spaces. In these depth intervals, traces of dissolved sulfate have been analyzed by Stopelli et al. (2020). Glodowska et al. (2020b) has shown that sulfate-reducing as well as S-oxidizing microorganisms are present. These observations are in accordance with lobate grain boundaries of aged pyrite (Fig. 11c), indicating either sulfide oxidation or undersaturation of sulfide in the groundwater causing some re-dissolution of pyrite (Fig. 12). Fresh spherical framboids and aged pyrite with clearly discernable dissolution features occur at the same depth (e.g. 30 m, see Fig. 11), indicating successive steps of microbial sulfate and Fe reduction, and S oxidation. This observation suggests an active S cycle and confirms oscillation of redox conditions, which is also suggested by the cyclic precipitation of Fe (oxyhydr)oxides.

5.3 Mobilization and immobilization of As within the redox interfaces

The various Fe phases that were identified at the redox interfaces differ in their interaction with As and thus in their immobilization potential. The highest As concentrations of up to 5800 $\mu\text{g/g}$ were measured in framboidal pyrite (Fig. 11b) but as described above, the abundance of pyrite is low in the investigated redox interfaces throughout the aquifer. Pyrite has only been observed at 22 and 30 m depth and along preferential flow paths in the sediment. Nevertheless, this finding confirms all previous studies arguing that pyrite is most efficient in As(III) immobilization (e.g. Lowers et al., 2007; Le Pape et al., 2017; Wang et al., 2018; Phan et al., 2019). However, we also observed dissolution of pyrite (Fig. 11c). Although the importance of authigenic pyrite as sink for As and its redistribution into pyrite during diagenesis is significant because of the high storage capacity of pyrite for As (Lowers et al., 2007), its role for the entire As budget in the investigated aquifer at Van Phuc, Vietnam, seem to be minor because of their low abundance. We have observed dissolution of aged pyrite (Fig. 11c), which therefore indicates that pyrite could rather be a source of dissolved As in gray aquifer sands.

Iron-bearing carbonates, which were frequently observed in the sandy aquifer, can also incorporate As (e.g. Guo et al., 2007). Their importance in removing As from the reduced plume is relatively low compared to the other Fe minerals found at the redox transition with concentrations mostly below the detection limit of the electron microprobe. But higher spatial resolution methods should be applied as Fe carbonates with concentrations in the range $<70 \mu\text{g/g}$ might also have a high As immobilization potential if Fe carbonate precipitation is widespread. However, their alteration rims are characterized by newly formed Fe phyllosilicates and Fe (oxyhydr)oxides with slightly higher As concentrations (140 $\mu\text{g/g}$; Fig.

6a). This observation suggests that even Fe-bearing carbonates underwent mineral transformations under more oxidizing conditions, and indicates that alteration rims around Fe-bearing carbonates are a significant sink for As.

The Fe precipitates, occurring as mineral coatings and cementations of pore spaces in the redox transition zones, show As concentrations in the range 70 to 500 µg/g. We observed a tendency towards higher As concentrations in fresh, goethite-rich Fe precipitates and lower As concentrations in aged magnetite/hematite-enriched precipitates (Fig. 8). This indicates that these precipitates might become a source of As upon aging. Redox oscillations are also visible in the As speciation. While the As(III) content is significantly higher in goethite coatings, the ratio of As(III):As(V) is more equal in the central part of cementations composed of hematite and magnetite (Fig. 10).

The presented conceptual model of the dynamic Fe mineralogy at redox transition zones in sandy aquifers of the Red River delta (Vietnam) very well explains the (im)mobilization behavior of As, not only in groundwater of the studied area but also provides an explanation for the Fe and As dynamics at redox transition zones elsewhere in As-affected aquifers of south and southeast Asia.

6. CONCLUSION

We investigated the microscale Fe mineralogy and their potential for As (im)mobilization at redox interfaces in a sand aquifer of the Red River, Vietnam, where high and low As concentrations in groundwater are juxtaposed (D in Fig. 1b). Due to the intrusion of reduced groundwater from Holocene into Pleistocene sands and microbially driven methanogenesis of organic matter, reductive dissolution of As-bearing goethite releases Fe^{2+} and As into solution (van Geen et al., 2013; Stopelli et al., 2020; Glodowska et al., 2020b). Near the top and bottom aquitard and within the sand aquifer we observed strong color changes on mm- to cm-scales. These redox interfaces are mostly characterized by sharp gradients in grain size, magnetic susceptibility and chemical composition (Fe_2O_3 , As, TS, TC and P_2O_5). This observation suggests that the permeability and local groundwater flow conditions are responsible for establishing redox interfaces and regulate the formation of secondary Fe phases.

Our study revealed that the transformation of orange sand (As uncontaminated) to yellow-brown (sand aquifer between 30 and 40 m) and gray sand (aquifer between 20 and 30 m) occurs via coupled redox reactions with siderite as an important secondary Fe mineral, although with a low capacity for As immobilization. The rusty-orange color of these zones is related to newly

precipitated Fe (oxyhydr)oxides, which immobilized significant amounts of As, either as As(III) or As(V) species. The presumably microbially-driven formation of micro- to nanocrystalline Fe mineral precipitates leads to a considerable adsorption or incorporation of both As species. Consequently, these precipitates characterize the redox interfaces as active hotspots and zones of enhanced As immobilization.

Precipitation and dissolution of reduced phases like Fe-bearing carbonates and pyrite and the new formation of Fe (oxyhydr)oxides and their redox reactions (goethite - magnetite) clearly indicate a high redox dynamic at these redox interfaces. We refined with our results existing conceptual models explaining the source and sink mechanisms for As (im)mobilization within sandy aquifers of deltaic sediments in south and southeast Asia, which helps to understand the migration dynamics of redox transition zones.

Acknowledgements -This work was funded by the Deutsche Forschungsgemeinschaft DFG (project NE687/8-1: Retardation and mobilization of As at redox fronts under advective flow conditions – a concerted multidisciplinary approach (AdvectAs)) and the Swiss National Science Foundation SNF (grant 200021E-167821). We also thank Beate Oetzel, Ferry Schiperski and Viktor Dück for XRD measurements and evaluations, Andreas Grün for grain size analysis and magnetic investigations, and Kristian Nikolowski for thin section preparation. We would like to thank Yan Zheng, Lex van Geen and anonymous who helped to improve the clarity of this manuscript with their thorough reviews.

REFERENCES

- Akai J., Izumi K., Fukuhara H., Masuda H., Nakano S., Yoshimura T., Ohfuji H., Anawar H.M. and Akai K. (2004) Mineralogical and geomicrobiological investigations on groundwater arsenic enrichment in Bangladesh. *Applied Geochemistry* **19** (2), 215–230.
- Aromokeye D.A., Kulkarni A.C., Elvert M., Wegener G., Henkel S., Coffinet S., Eickhorst T., Oni O.E., Richter-Heitmann T., Schnakenberg A., Taubner H., Wunder L., Yin X., Zhu Q., Hinrichs K.U., Karsten S., and Friedrich M.W. (2020) Rates and Microbial Players of Iron-Driven Anaerobic Oxidation of Methane in Methanic Marine Sediments, *Front. Microbiol.* **10**. <https://doi.org/10.3389/fmicb.2019.03041>.
- Beal E.J., House C.H., and Orphan V.J. (2009) Manganese- and Iron-Dependent Marine Methane Oxidation. *Science* **325**, 184–187. <https://doi.org/10.1126/science.1169984>.
- Benner S.G., and Fendorf S. (2010) Arsenic in South Asia Groundwater. *Geography Compass* **4** (10), 1532–1552.
- Berg M., Tran H.C., Nguyen T.C., Pham H.V., Schertenleib R., Giger W. (2001) Arsenic contamination of groundwater and drinking water in Vietnam. A human health threat. *Environ Sci Technol* **35** (13), 2621–2626.

- 729 Berg M., Stengel C., Trang P.T.K., Viet P.H., Sampson, M.L., Leng M., Samreth S. and
730 Fredericks D. (2007) Magnitude of arsenic pollution in the Mekong and Red River Deltas--
731 Cambodia and Vietnam. *The Science of the total environment* **372** (2-3), 413–425. DOI:
732 10.1016/j.scitotenv.2006.09.010.
- 733 Berg M., Trang P.T.K., Stengel C., Buschmann J., Viet P.H., van Dan N., Giger W. and Stüben
734 D. (2008): Hydrological and sedimentary controls leading to arsenic contamination of
735 groundwater in the Hanoi area, Vietnam. The impact of iron-arsenic ratios, peat, river bank
736 deposits, and excessive groundwater abstraction. *Chemical Geology* **249** (1-2), 91–112.
737 DOI: 10.1016/j.chemgeo.2007.12.007.
- 738 Berquó T.S., Banerjee S.K., Ford R.G., Penn R.L. and Pichler T. (2007) High crystallinity Si-
739 ferrihydrite. An insight into its Néel temperature and size dependence of magnetic
740 properties. *J Geophys Res* **112**, B02102. DOI: 10.1029/2006JB004583.
- 741 Bostick B.C. and Fendorf S. (2003) Arsenite sorption on troilite (FeS) and pyrite (FeS₂).
742 *Geochim Cosmochim Acta* **67** (5), 909–921. DOI: 10.1016/S0016-7037(02)01170-5.
- 743 Chen G., Hofstetter T.B. and Gorski C.A. (2020) Role of carbonate in thermodynamic
744 relationships describing pollutant reduction kinetics by iron oxide-bound Fe²⁺. *Environ Sci*
745 *Technol* **54**, 10109–10117. DOI: 10.1021/acs.est.0c02959.
- 746 Coker V.S., Gault A.G., Pearce C.I., van der Laan G., Telling N.D., Charnock J.M., Polya D.A.,
747 Lloyd J.R. (2006) XAS and XMCD evidence for species-dependent partitioning of arsenic
748 during microbial reduction of ferrihydrite to magnetite. *Environ Sci Technol* **40**, 7745–7750.
- 749 Cornell R.M. and Schwertmann U. (2003) The iron oxides. Structure, properties, reactions,
750 occurrences, and uses. 2nd, completely rev. and extended ed. Weinheim: Wiley-VCH.
- 751 Cudennec Y. and Lecerf A. (2006) The transformation of ferrihydrite into goethite or hematite,
752 revisited. *Journal of Solid State Chemistry* **179**, 716–722.
- 753 Dowling C.B., Poreda R.J., Basu A.R., Peters S.L. and Aggarwal P.K. (2002) Geochemical
754 study of arsenic release mechanisms in the Bengal Basin groundwater. *Water Resour Res* **38**
755 (9), 12-1-12-18. DOI: 10.1029/2001WR000968.
- 756 Dunlop D.J. and Özdemir Ö. (1997) Rock magnetism – fundamentals and frontiers. Cambridge
757 University Press, 573 pp.
- 758 Eiche E., Berg M., Hönig S.-M., Neumann T., Lan V.M., Trang P.T.K. and Viet P.H. (2017)
759 Origin and availability of organic matter leading to arsenic mobilisation in aquifers of the
760 Red River Delta, Vietnam. *Applied Geochemistry* **77**, 184–193. DOI:
761 10.1016/j.apgeochem.2016.01.006.
- 762 Eiche E., Neumann T., Berg M., Weinman B., van Geen A., Norra S., Berner Z., Trang P.K.T.,
763 Viet P.H. and Stüben D. (2008) Geochemical processes underlying a sharp contrast in
764 groundwater arsenic concentrations in a village on the Red River delta, Vietnam. *Applied*
765 *Geochemistry* **23** (11), 3143–3154. DOI: 10.1016/j.apgeochem.2008.06.023.
- 766 Fendorf S., Michael H.A. and van Geen A. (2010) Spatial and temporal variations of
767 groundwater arsenic in South and Southeast Asia. *Science* **328**, 1123–1127. DOI:
768 10.1126/science.1172974.
- 769 Funabiki A., Haruyama S., van Quy N., van Hai P. and Thai D.H. (2007) Holocene delta plain
770 development in the Song Hong (Red River) delta, Vietnam. *Journal of Asian Earth Sciences*
771 **30**, 518–529. DOI: 10.1016/j.jseas.2006.11.013.
- 772 Giménez J., Martínez M., de Pablo J., Rovira M. and Duro L. (2007) Arsenic sorption onto
773 natural hematite, magnetite, and goethite. *Journal of Hazardous Materials* **141**, 575–580.

- 774 Glodowska M., Stopelli E., Schneider M., Lightfoot A., Rathi B., Straub D., Patzner M., Duyen
775 V. T., Berg M., Kleindienst S. and Kappler A. (2020a) Role of in Situ Natural Organic
776 Matter in Mobilizing As during Microbial Reduction of FeIII-Mineral-Bearing Aquifer
777 Sediments from Hanoi (Vietnam). *Environ Sci Technol*. DOI: 10.1021/acs.est.9b07183.
- 778 Glodowska M., Stopelli E., Straub D., Vu Thi D., Trang P.T.K, Viet P.H., AdvectAs team
779 members, Berg M., Kappler A., Kleindienst S. (2020b) Arsenic behaviour in groundwater
780 in Hanoi (Vietnam) influenced by a complex biogeochemical network of iron, methane, and
781 sulfur cycling. *Journal of Hazardous Materials*. DOI: 10.1016/j.jhazmat.2020.12439.
- 782 Glodowska M., Stopelli E., Schneider M., Rathi B., Straub D., Lightfoot A., Kipfer R., Berg M.,
783 Jetten M., Kleindienst S., Kappler A. and AdvectAs Team Members (2020c) Arsenic
784 mobilization by anaerobic iron-dependent methane oxidation. *Commun Earth Environ* **1**, 42.
785 DOI.org/10.1038/s43247-020-00037-y.
- 786 Guo H.M., Stüben D. and Berner Z. (2007) Removal of arsenic from aqueous solution by
787 natural siderite and hematite. *Appl Geochem* **22**, 1039–1051.
- 788 Guyodo Y., Mostrom A., Lee P.R. and Banerjee S.K. (2003) From Nanodots to Nanorods.
789 Oriented aggregation and magnetic evolution of nanocrystalline goethite. *Geophys Res Lett*
790 **30** (10), 1512. DOI: 10.1029/2003GL017021.
- 791 Hansel C.M., Benner S.G. and Fendorf S. (2005) Competing Fe (II)-induced mineralization
792 pathways of ferrihydrite. *Environ Sci Technol* **39** (18), 7147–7153. DOI:
793 10.1021/es050666z.
- 794 Harvey C.F., Swartz C.H., Badruzzaman A.B.M., Keon-Blute N., Yu W., Ali M.A., Jay J.,
795 Beckie R., Niedan V., Brabander D., Oates P.M., Ashfaq K.N., Islam S., Hemond H.F.
796 and Ahmed M.F. (2002) Arsenic mobility and groundwater extraction in Bangladesh.
797 *Science* **298**, 1602–1606. DOI: 10.1126/science.1076978.
- 798 Horneman A., van Geen A., Kent D.V., Mathe P.E., Zheng Y., Dhar R.K., O’Connell S., Hoque
799 M.A., Aziz Z., Shamsudduha M., Seddique A.A. and Ahmed K.M. (2004) Decoupling of As
800 and Fe release to Bangladesh groundwater under reducing conditions. Part 1: Evidence from
801 sediment profiles. *Geochim Cosmochim Acta* **68** (17), 3459–3473.
- 802 Huang P.M., Oscarson D.W., Liaw W.K. and Hammer U.T. (1982) Dynamics and mechanisms
803 of arsenite oxidation by freshwater lake sediments. *Hydrobiologia* **91**, 315–322.
- 804 Islam F.S., Gault A.G., Boothman C., Polya D.A., Charnock J.M., Chatterjee D. and Lloyd J.R.
805 (2004) Role of metal-reducing bacteria in arsenic release from Bengal delta sediments.
806 *Nature* **430** (6995), 68–71. DOI: 10.1038/nature02638.
- 807 Jung H.B., Bostick B.C. and Zheng Y. (2012) Field, experimental, and modelling study of
808 arsenic partitioning across a redox transition in a Bangladesh aquifer. *Environ Sci Technol*
809 **46**, 1388–1395. DOI: 10.1021/es2032967.
- 810 Jung H.B., Zheng Y., Rahman M.W., Rahman M.M. and Ahmed K.M. (2015) Redox zonation
811 and oscillation in the hyporheic zone of the Ganges-Brahmaputra-Meghna delta:
812 implications for the fate of groundwater arsenic during discharge. *Appl Geochem* **63**, 647–
813 660. DOI: 10.1016/j.apgeochem.2015.09.001.
- 814 Le Pape P., Blanchard M., Brest J., Boulliard J.-C., Ikogou M., Stetten L., Wang S., Landrot G.
815 and Morin G. (2017) Arsenic Incorporation in Pyrite at Ambient Temperature at Both
816 Tetrahedral S-I and Octahedral FeII Sites. Evidence from EXAFS-DFT Analysis. *Environ*
817 *Sci Technol* **51** (1), 150–158. DOI: 10.1021/acs.est.6b03502.
- 818 Li Y.-L., Zhu S.-Y. and Deng K. (2011) Mössbauer hyperfine parameters of iron species in the
819 course of *Geobacter*-mediated magnetite mineralization. *Phys Chem Minerals* **38**, 701–708.

820 Li, Y., Yang, M., PEntrak, M., He, H., Arai, Y. (2020). Carbonate-enhanced Transformation of
821 Ferrihydrite to Hematite. *Environ. Sci. Technol.* **54**, 13701–13708.

822 Liu Q., Yu Y., Muxworthy A.R. and Roberts A.P. (2008) Effects of internal stress on remanence
823 intensity jumps across the Verwey transition for multi-domain magnetite. *Phys Earth Planet*
824 *Inter* **169**, 100–107.

825 Lowers H.A., Breit G.N., Foster A.L., Whitney J., Yount J., Uddin M.N. and Muneem A.A.
826 (2007) Arsenic incorporation into authigenic pyrite, Bengal Basin sediment, Bangladesh.
827 *Geochim Cosmochim Acta* **71**, 2699–2717. DOI: 10.1016/j.gca.2007.03.022.

828 Mayer T.D. and Jarrell W.M. (2000) Phosphorus sorption during iron(II) oxidation in the
829 presence of dissolved silica. *Water research* **34** (16), 3949–3956. DOI: 10.1016/S0043-
830 1354(00)00158-5.

831 McArthur J.M., Ravenscroft P., Safiulla S. and Thirlwall M.F. (2001) Arsenic in groundwater.
832 Testing pollution mechanisms for sedimentary aquifers in Bangladesh. *Water Resour Res* **37**
833 (1), 109–117. DOI: 10.1029/2000WR900270.

834 Neidhardt H., Berg M., Stengel C., Winkel L., Kaegi R., Trang, P.T.K., Lan V.T.M., Thao
835 M.T.P. and Viet P.H. (2014) Arsenic adsorption on iron mineral phases under reducing
836 conditions. In: Marta Litter, Hugo Nicolli, Martin Meichtry, Natalia Quici, Jochen
837 Bundschuh, Prosun Bhattacharya und Ravi Naidu (Hg.): One Century of the Discovery of
838 Arsenicosis in Latin America (1914–2014) As2014, Bd. 20142152: CRC Press (Arsenic in
839 the Environment - Proceedings), 83–84.

840 Neidhardt H., Winkel L.H.E., Kaegi R., Stengel C., Trang, P.T.K., Lan V.M., Viet P.H. and
841 Berg M. (2018) Insights into arsenic retention dynamics of Pleistocene aquifer sediments by
842 in situ sorption experiments. *Water research* **129**, 123–132. DOI:
843 10.1016/j.watres.2017.11.018.

844 Nghiem A.A., Stahl M.O., Mailloux B.J., Mai T.T., Trang P.T., Viet P.H. Harvey C.F., van
845 Geen, A., Bostick B.C. (2019) Quantifying Riverine Recharge Impacts on Redox Conditions
846 and Arsenic Release in Groundwater Aquifers Along the Red River, Vietnam. *Water Resour*
847 *Res* **55** (8), 6712–6728. DOI: 10.1029/2019WR024816.

848 Nghiem A.A., Shen Y., Stahl M.O., Sun J., Haque E., DeYoung B., Nguyen K.N., Mai T.T.,
849 Trang P.T.K., Viet P.H., Mailloux B.J., Harvey C.F., van Geen, A. and Bostick B.C. (2020)
850 Aquifer-scale observations of iron redox transformations in arsenic-impacted environments
851 to predict future contamination. *Environ Sci Technol* **XX**, xxx-xxx. DOI:
852 10.1021/acs.estlett.0c00672.

853 Nickson R.T., McArthur J.M., Ravenscroft P., Burgess W.G. and Ahmed K.M. (2000)
854 Mechanism of arsenic release to groundwater, Bangladesh and West Bengal. *Applied*
855 *Geochemistry* **15** (4), 403–413. DOI: 10.1016/S0883-2927(99)00086-4.

856 Oscarson D.W., Huang P.M. and Liaw W.K. (1980) The oxidation of arsenite by aquatic
857 sediments. *Journal of Environmental Quality* **9** (4), 700–703. DOI:
858 10.2134/jeq1980.00472425000900040032x.

859 Phan V.T.H., Bernier-Latmani R., Tisserand D., Bardelli F., Le Pape P. and Fruttschi M. (2019)
860 As release under the microbial sulfate reduction during redox oscillations in the upper
861 Mekong delta aquifers, Vietnam. A mechanistic study. *The Science of the total environment*
862 **663**, 718–730. DOI: 10.1016/j.scitotenv.2019.01.219.

863 Postma D. and Jakobsen R. (1996) Redox zonation. Equilibrium constraints on the Fe(III)/SO₄-
864 reduction interface. *Geochim Cosmochim Acta* **60** (17), 3169–3175. DOI: 10.1016/0016-
865 7037(96)00156-1.

- 866 Postma D., Jessen S., Hue N.T.M., Duc M.T., Koch C.B., Viet P.H., Nhan P.Q. and Larsen F.
867 (2010) Mobilization of arsenic and iron from Red River floodplain sediments, Vietnam.
868 *Geochim Cosmochim Acta* **74** (12), 3367–3381. DOI: 10.1016/j.gca.2010.03.024.
- 869 Postma D., Larsen F., Minh Hue N.T., Duc M.T., Viet P.H., Nhan P.Q. and Jessen S. (2007)
870 Arsenic in groundwater of the Red River floodplain, Vietnam. Controlling geochemical
871 processes and reactive transport modeling. *Geochim Cosmochim Acta* **71** (21), 5054–5071.
872 DOI: 10.1016/j.gca.2007.08.020.
- 873 Postma D., Larsen F., Thai N.T., Trang P.T.K., Jakobsen R. Nhan P.Q., Long T.V., Viet P.H.
874 & Murray A.S. (2012) Groundwater arsenic concentrations in Vietnam controlled by
875 sediment age. *Nature Geosci* **5** (9), 656–661. DOI: 10.1038/ngeo1540.
- 876 Rancourt D.G. and Ping J.Y. (1991) Voigt-based methods for arbitrary-shape static hyperfine
877 parameter distributions in Mössbauer spectroscopy. *Nuclear Instruments and Methods in*
878 *Physics Research Section B: Beam Interactions with Materials and Atoms* **58** (1), 85–97.
879 DOI: 10.1016/0168-583X(91)95681-3.
- 880 Rathi B., Neidhardt H., Berg M., Siade A. and Prommer H. (2017) Processes governing arsenic
881 retardation on Pleistocene sediments. Adsorption experiments and model-based analysis. In:
882 *Water Resour Res* **53** (5), S. 4344–4360. DOI: 10.1002/2017WR020551.
- 883 Ravel B. and Newville M. (2005) ATHENA, ARTEMIS, HEPHAESTUS: data analysis for X-
884 ray absorption spectroscopy using IFEFFIT. *Journal of Synchrotron Radiation* **12**, 537–541
885 (2005) doi:10.1107/S0909049505012719.
- 886 Ravenscroft P., Brammer H., and Richards K. (2009) Arsenic Pollution. Oxford, UK: Wiley-
887 Blackwell.
- 888 Roberts L.C., Hug S.J., Ruettimann T., Billah M., Khan A.W. and Rahman M.T. (2004) Arsenic
889 removal with iron(II) and iron(III) in waters with high silicate and phosphate concentrations.
890 *Environmental science & technology* **38** (1), 307–315. DOI: 10.1021/es0343205.
- 891 Sanchez-Roman M., Puente-Sanchez F., Parro V. and Amils R. (2015) Nucleation of Fe-rich
892 phosphates and carbonates on microbial cells and exopolymeric substances. *Frontiers in*
893 *Microbiology* **6**, 1024.
- 894 Sawlowicz Z. (1993) Pyrite framboids and their development. A new conceptual mechanism.
895 *Geol Rundsch* **82** (1), 148–156. DOI: 10.1007/BF00563277.
- 896 Schaefer M.V., Guo X., Gan Y., Benner S.G., Griffin A.M., Gorski C.A., Wang Y. and Fendorf
897 S. (2017) Redox controls on arsenic enrichment and release from aquifer sediments in central
898 Yangtze River Basin. *Geochim Cosmochim Acta* **204**, 104–119.
- 899 Senn A.-C., Hug S.J., Kaegi R., Hering J.G. and Voegelin A. (2018) Arsenate co-precipitation
900 with Fe(II) oxidation products and retention or release during precipitate aging. *Water*
901 *research* **131**, 334–345. DOI: 10.1016/j.watres.2017.12.038.
- 902 Smedley P.L and Kinniburgh D.G (2002) A review of the source, behaviour and distribution of
903 arsenic in natural waters. *Applied Geochemistry* **17** (5), S. 517–568. DOI: 10.1016/S0883-
904 2927(02)00018-5.
- 905 Stahl M.O., Harvey C.F., van Geen A., Sun J., Thi Kim Trang P., Mai Lan V., Phuong T.M.,
906 Viet P.H., Bostick B.C. (2016) River bank geomorphology controls groundwater arsenic
907 concentrations in aquifers adjacent to the Red River, Hanoi Vietnam. *Water Resour Res* **52**
908 (8), 6321–6334. DOI: 10.1002/2016WR018891.
- 909 Stopelli E., Duyen V.T., Mai, Tran T., Trang P.T.K., Viet P.H., Lightfoot, A., Kipfer R.,
910 Schneider M., Eiche E., Kontny A., Neumann T., Glodowska M., Patzner M., Kappler A.,

911 Kleindienst S., Rathi B., Cirpka O., Bostick B., Berg M. (2020): Spatial and temporal
 912 evolution of groundwater arsenic contamination in the Red River delta, Vietnam. Interplay
 913 of mobilisation and retardation processes. *The Science of the total environment* **717**, 137143.
 914 DOI: 10.1016/j.scitotenv.2020.137143.

915 Stuckey J.W., Schaefer M.V., Kocar B.D., Dittmar J., Pacheco J.L., Benner S.G. and Fendorf
 916 S. (2015) Peat formation concentrates arsenic within sediment deposits of the Mekong Delta.
 917 *Geochim Cosmochim Acta* **149**, 190–205. DOI: 10.1016/j.gca.2014.10.021.

918 Sultan R.F., Abdel-Fattah and Abdel-Rahman M. (2013) On dynamic self-organization.
 919 Examples from magmatic and other geochemical systems. *Lat Am J Solids Struct* **10** (1), 59–
 920 73. DOI: 10.1590/S1679-78252013000100006.

921 Swartz C.H., Blute N.K., Badruzzman B., Ali A., Brabander D., Jay J., Besancon J., Islam S.,
 922 Hemond H.F., Harvey C.F. (2004) Mobility of arsenic in a Bangladesh aquifer. Inferences
 923 from geochemical profiles, leaching data, and mineralogical characterization. *Geochim*
 924 *Cosmochim Acta* **68** (22), 4539–4557. DOI: 10.1016/j.gca.2004.04.020.

925 Tarling D.H. and Hrouda F. (1993) The magnetic anisotropy of rocks. Chapman and Hall,
 926 London, p 215.

927 Till J. and Nowaczyk N. (2018) Authigenic magnetite formation from goethite and hematite
 928 and chemical remanent magnetization acquisition. *Geophysical Journal International* **213**
 929 (3), 1818-1831.

930 Van Geen A., Rose J., Thorai S., Garnier J.M., Zheng Y. and Bottero J.Y. (2004) Decoupling
 931 of As and Fe release to Bangladesh groundwater under reducing conditions. Part II: Evidence
 932 from sediment incubations. *Geochim Cosmochim Acta* **68** (17), 3475–3486.

933 Van Geen A., Bostick B.C., Trang P.T.K., Lan V.M., Mai N., Manh P.D., Viet P.H., Radloff
 934 K., Aziz Z., Mey J.L., Stahl M.O., Harvey C.F., Oates P., Weinman B., Stengel C., Frei F.,
 935 Kipfer R. & Berg M. (2013): Retardation of arsenic transport through a Pleistocene aquifer.
 936 *Nature* 501 (7466), 204–207. DOI: 10.1038/nature12444.

937 Voegelin A., Kaegi R., Frommer J., Vantelon D., Hug S.J. (2010) Effect of phosphate, silicate,
 938 and Ca on Fe(III)-precipitates formed in aerated Fe(II)- and As(III)-containing water studied
 939 by X-ray absorption spectroscopy. *Geochim Cosmochim Acta* **74** (1), 164–186. DOI:
 940 10.1016/j.gca.2009.09.020.

941 Voegelin A., Senn A.-C., Kaegi R. and Hug S.J. (2019) Reductive dissolution of As(V)-bearing
 942 Fe(III)-precipitates formed by Fe(II) oxidation in aqueous solutions. *Geochemical*
 943 *transactions* **20** (1), S. 2. DOI: 10.1186/s12932-019-0062-2.

944 Voegelin A., Senn A.-C., Kaegi R., Hug S.J., and Mangold S. (2013) Dynamic Fe-precipitate
 945 formation induced by Fe(II) oxidation in aerated phosphate-containing water. *Geochim*
 946 *Cosmochim Acta* **117**, 216–231. DOI: 10.1016/j.gca.2013.04.022.

947 Wallis I., Pommer H., Berg M., Siade A.J., Sun J. and Kipfer R. (2020) The river-groundwater
 948 interface as a hotspot for arsenic release. *Nature Geoscience* **13**, 288-295

949 Wang Y., Le Pape P., Morin G., Asta M.P., King G., Bártoová B., Suvorova E., Fruttschi M.,
 950 Ikogou M., Pham V.H.C, Vo P.L., Herman F., Charlet L. and Bernier-Latmani R. (2018):
 951 Arsenic Speciation in Mekong Delta Sediments Depends on Their Depositional
 952 Environment. *Environmental science & technology* **52** (6), 3431–3439. DOI:
 953 10.1021/acs.est.7b05177.

954 Wang H., Byrne J., Benning L., Thomas A., Göttlicher J., Höfer H., Mayanna S., Perez J.,
 955 Kontny A., Kappler A., Guo H. and Norra S. (2020) Arsenic sequestration in pyrite and

- greigite in the buried peat of As-contaminated aquifers. *Geochim Cosmochim Acta* **284**, 107–119.
- Wilkin R.T., Barnes H.L. and Brantley S.L. (1996) The size distribution of framboidal pyrite in modern sediments. An indicator of redox conditions. *Geochim Cosmochim Acta* **60** (20), 3897–3912. DOI: 10.1016/0016-7037(96)00209-8.
- Winkel L.H.E., Pham T.K.T., Vi M.L., Stengel C., Amini M., Nguyen T.H., Viet P.H. and Berg M. (2011) Arsenic pollution of groundwater in Vietnam exacerbated by deep aquifer exploitation for more than a century. *Proceedings of the National Academy of Sciences of the United States of America* **108** (4), 1246–1251. DOI: 10.1073/pnas.1011915108.
- Zheng Y., van Geen, A., Stute M., Dhar R., Mo Z., Cheng Z., Horneman A., Gavrieli I., Simpson H.J., Versteeg R., Steckler M., Grazioli-Venier A., Goodbred S., Shahnewaz M., Shamsudduha M., Hoque M.A. and Ahmed K.M. (2005) Geochemical and hydrogeochemical contrasts between shallow and deeper aquifers in two villages of Arai-hazar, Bangladesh: implications for deeper aquifers as drinking water sources. *Geochim Cosmochim Acta* **69** (22), 5203–5218.
- Zhu T. and Dittrich M. (2016) Carbonate Precipitation through Microbial Activities in Natural Environment, and Their Potential in Biotechnology. A Review. *Frontiers in bioengineering and biotechnology* **4**, 4. DOI: 10.3389/fbioe.2016.00004.

Figure Captions

Fig. 1. a) Hanoi region with the village of Van Phuc in the Red River delta. Contour lines indicate groundwater heads in the Pleistocene aquifer (from Berg et al., 2008). b) Satellite view of Van Phuc showing the southeast to northwest transect (white line) studied by van Geen et al. (2013). Symbol color distinguishes the Holocene aquifer with high As (red marks), the Pleistocene aquifer with low As (cyan marks, $<10 \mu\text{g/L}$), and the transition zone where high (yellow) and low (green) dissolved As concentrations occur within 20-30 m (modified from van Geen et al. 2013). The investigated core RD42 is marked by the purple cross in the redox transition zone D. c) Groundwater flow direction. The transition zone is expected to move to the NW due to heavy groundwater abstraction in the city of Hanoi (modified after van Geen et al., 2013). A-E are hydrogeochemical zones from Stopelli et al. (2020).

Fig. 2. Sediment core RD42 with Munsell soil color charts, grain size distribution ($n=78$), magnetic susceptibility (k ; $n=349$) and concentration of selected elements ($n=74$). Note that MnO, TC and TS have a logarithmic scale for better visibility, and k is cut off at $1000 \times 10^{-6} \text{ SI}$ for scale issues. The sand aquifer comprises the redox transition zone (shown as zone D in Fig. 1b) with numerous small-scale redox interfaces shown in Fig. 3.

Fig. 3. Sediment cores from the sand aquifer with small-scale redox interfaces (dashed rectangles) at 20 m, 21 m, 30 m and 41m, indicated as orange transition zones in Fig. 2. a) A massive Fe-concretion stretching from 19.6 to 20 m depth marks the transition from the upper aquitard to the aquifer below. b) At a depth of 21 m, the sandy sediments show a red-brown to beige banding over ca. 15 cm indicating mm to cm-scale redox changes. c) At a depth of 30 m, the sediments are coarser but still show a faint color banding indicative for redox interfaces. Above this zone, the characteristic orange color decreases significantly and turns into greyish color upwards and yellow-brown color downwards (see SI2). d) The redox interface in the lower aquifer-aquitards transition at 41 m depth extend over ca. 10 cm. Their strong orange color clearly distinguishes them from all other sediments outside the redox interface zone. The hole within the dashed rectangle indicates a spot for bulk sampling. The white frame shows the position for the thin section shown in (e). (e) Thin section with redox interface at 41 m and well exposed clusters of Fe-(oxyhydr)oxide precipitations (marked by white arrow) on the less reduced side of the redox interface. This area was chosen for combined EPMA and μXANES analysis (see Fig. 8-10).

Fig. 4. Temperature dependent magnetic susceptibility (normalized to value at room temperature) from different depths in the sand aquifer. Heating curve is indicated in black and cooling curve in dotted gray. (a) Magnetite with Verwey transition (T_V) and Curie temperature (T_C). (b) In the transition zone at 30 m depth, Fe-carbonate is seen in the heating curve. (c) Transformation of lepidocrocite (T_{t1}) into magnetite. (d) Transformation of lepidocrocite (T_{t1}) and Fe-carbonate (T_{t2}) into magnetite. Inlay shows a strong drop in magnetic susceptibility at low temperature indicating goethite or ferrihydrite and little magnetite (T_V). (e) and (f) show reference curves for lepidocrocite and siderite. Note that siderite is probably not pure but contains some Mn. This is indicated by the T_C in the cooling curve, which is lower compared to pure magnetite.

Fig. 5. Mössbauer spectra and fits for samples from different depths in the sand aquifer at (a) 77 K and (b) 5 K. Ordered goethite (green) and lepidocrocite/ferrihydrite (gray, indicated as Fe(III) in the figure) are the major phases. Hematite was identified in the yellow-brown sand at 30.0 and 36.4 m.

Fig. 6. Scanning electron micrographs of different Fe carbonate textures from the RTZ at 21 m depth (compare Fig. 3b). (a) Spherical Fe carbonate grain with a rim of phyllosilicates and Fe oxides shows higher As concentration compared to the Fe carbonate core. Numbers indicate $\mu\text{g As/g}$. (b) Fe carbonate aggregate cementing quartz and feldspar fragments. (c) Siderite cementation with skeletal growth.

Fig. 7. Scanning electron micrographs of a spherical Fe-rich carbonate grain from 21 m depth with As concentrations (in $\mu\text{g/g}$) close to the detection limit, and elemental mapping images of Mn, Ca, Al, P, O, Fe, As. The brightened rectangle in the SEM image marks the area for element mapping. Note the increase of Al, Fe, O and P content along the grain rim, indicating the transformation of carbonate into a Fe-, P-, Al-, O-rich phase.

Fig. 8. Scanning electron micrographs of Fe (oxyhydr)oxide precipitates occurring as coatings (a-d) at 41 m depth. (a) Sub-rounded grains of quartz (Qz), feldspar (Fsp), partly as lithic fragments intergrown with various phyllosilicates (PS; e.g. muscovite and chlorite) with rims of Fe oxides/hydroxides. (b) Rim shows a zonation with magnetite/hematite (bright gray/white

gray) in the inner part and goethite (gray) in the outer part of the rim. (c) Hedgehog-like morphologies of goethite with a core of magnetite/hematite. Numbers give $\mu\text{g As/g}$. (d) Delicate mineral structures resembling those produced by bacteria (e.g. Voegelin et al., 2013).

Fig. 9. Scanning electron micrographs of Fe precipitates occurring as cementations (a-c) at 41 m depth. (a) Quartz and lithic fragments are cemented by Fe precipitates. Magnification of white frame in (b) shows different textures of the Fe (oxyhydr)oxides. (c) Gel like Fe-precipitates (gray: goethite, bright gray: magnetite/hematite) with oscillating morphologies from area labelled by frame in (b). Numbers give As concentration in $\mu\text{g/g}$. Elemental mapping images of Ca, S, P, Fe, Al, O are given for area labelled by white frame in (c).

Fig. 10. Photomicrograph of Fe precipitates cementing quartz and lithic fragments from 41 m depth (a). (b) and (c) show close-ups from cementations (b) and coatings (c). (d) μXANES analyses at the Fe K-edge at spots marked by red and blue crosses in (b) and (c), and of goethite (Gt), magnetite (Mt), hematite (Hem) as reference compounds. (e) As K-edge μXANES spectra of As(III) and As(V) and also from coatings and cementations. Note the different Gt : Hem and As(III) : As(V) ratio in the coatings (blue) and cementations (red).

Fig. 11. Scanning electron micrographs of pyrite framboids showing different developing stages from the transition zone at 30 m depth. (a) Spherical framboid with octahedral crystals, (b) framboid with cubic crystals, (c) slightly angular pyrite euhedra with lobate grain boundaries and microcracks, (d) irregular pyrite framboids arranged along a fluid pathway. Numbers in (b) and (c) show $\mu\text{g As/g}$ measured by EPMA.

Fig. 12. Conceptual model of Fe mineral transformations in the redox transition zones of the sandy aquifer integrating known mechanisms with the results of this study. Reductive dissolution causes a partial dissolution of Fe (oxyhydr)oxide coatings, but they can still be active in microenvironments for further coupled redox reactions. Blue arrows indicate reduction, red arrows oxidation. Numbers in the sketch refer to numbers in the header. The following abbreviations are used for groundwater (GW), phyllosilicates (PS) and magnetite (Mt). Primary refers to minerals that are present in the yellow-brown sand, secondary refers to minerals that were formed in the redox interfaces.

1074 Table 1. Sediment type, dominant grain size and geochemistry of the aquitard and aquifer of
1075 sediment core RD42. Bold numbers give the average with the range in small numbers below.
1076 Note the increased As and Fe concentrations at the redox interfaces.

1077

1078 Table 2. Iron minerals in yellow-brown and gray sand, and at the redox interfaces (cf. Fig. 2).
1079 For each mineral, the identification methods are indicated. Gray shading distinguishes the Fe
1080 oxidation state.

1081

Table 1

n _{RD42}	unit	sediment type	dominant grain size	As	Fe ₂ O ₃	MnO	Al ₂ O ₃	CaO	P ₂ O ₅	TS	TC
				[µg/g]	[wt%]						
29	aqui-tard	beige to black top silt	silt (75%)	13.6 (7.18) 4.8-30.3	4.9 (1.77) 1.5-9.2	0.05 (.03) 0.02-0.09	15.2 (2.87) 9.4-20.6	0.62 (.53) 0.1-1.7	0.09 (.04) 0.04-0.18	0.111 (.22) 0.002-0.913	1.61 (2.52) 0.05-9.68
8	aquifer	grey sand	sand (66%)	2.6 (1.26) <1.0-4.9	1.4 (.32) 1.1-2	0.01 (.01) 0.01-0.03	5.3 (.90) 4.1-7.1	0.10 (.02) 0.08-0.13	0.03 (.01) 0.02-0.05	0.005 (.00) 0.004-0.005	0.03 (.01) 0.02-0.05
20		yellow-brown sand	sand (70%)	3.2 (1.50) 1.3-6.0	1.9 (.33) 1.1-2.3	0.06 (.17) 0.01-0.79	6.4 (1.50) 4.1-11.6	0.19 (.07) 0.1-0.3	0.04 (.01) 0.03-0.08	0.006 (.00) 0.003-0.009	0.04 (.02) 0.02-0.12
11		orange redox interface	sand (50%)	7.3 (3.87) 4.2-16.5	4.2 (2.68) 2.3-11.0	0.05 (.03) 0.03-0.11	9.8 (2.95) 6.1-16.2	0.28 (.18) 0.1-0.7	0.07 (.02) 0.03-0.09	0.010 (.01) 0.004-0.019	0.15 (.12) 0.04-0.39
6	aqui-tard	brown bottom silt	silt (79%)	7.8 (3.39) 4.3-14.7	6.3 (1.58) 3.5-8.6	0.08 (.04) 0.03-0.15	15.9 (2.72) 12.0-19.9	0.28 (.05) 0.2-0.34	0.11 (.05) 0.06-0.21	0.006 (.00) 0.004-0.009	0.20 (.16) 0.06-0.53

Table 2

Fe-minerals	formula	aquifer sand			methods				
		yellow -orange sand	redox interface	gray sand	Microscopy/ SEM/EMPA	XRD	μ-XANES	Magnetic	Mössbauer
Siderite (Sd)	Fe ²⁺ CO ₃	X	XXX		+	+	+	+	-
Ankerite (Ank)	Ca(Fe ²⁺ ,Mg,Mn)(CO ₃) ₂	X	XXX		+	-	-	+	-
Pyrite (Py)	Fe ²⁺ S ₂		XXX		+	+	+	-	-
Ilmenite (Ilm)	Fe ^{2+/3+} TiO ₃	XX	X	X	+	-	-	-	-
Magnetite (Mt)	Fe ²⁺ Fe ³⁺ ₂ O ₄	X	X	XX	+	+	+	+	-
Goethite (Gt)	alpha-Fe ³⁺ O(OH)	XX	XXX	X	+	+	+	+	+
Lepidocrocite (Lep)	gamma-Fe ³⁺ O(OH)		X		-	+	-	?	?
Ferrihydrite (Fh)	Fe ³⁺ ₁₀ O ₁₄ (OH) ₂	X	XXX		?	-	+	?	?
Hematite (Hem)	Fe ³⁺ ₂ O ₃	XX	XXX	X	+	+	+	+	+
Clinocllore (Clc)	(Mg,Fe ²⁺) ₅ Al(Si ₃ Al)O ₁₀ (OH) ₈	frequency linked to occurrence of fine-grained layers			+	+	-	-	+
Chamosite (Chm)	(Fe ²⁺ ,Mg,Fe ³⁺) ₅ Al(Si ₃ Al)O ₁₀ (OH,O) ₈				+	+	-		
Glaucanite (Glt)	(K,Na)(Fe ³⁺ ,Al,Mg) ₂ (Si,Al) ₄ O ₁₀ (OH) ₂				+	-	-		

X=rare, XX=moderate, XXX=abundant, + = present, ? = no clear evidence, - = not present

Figure 1

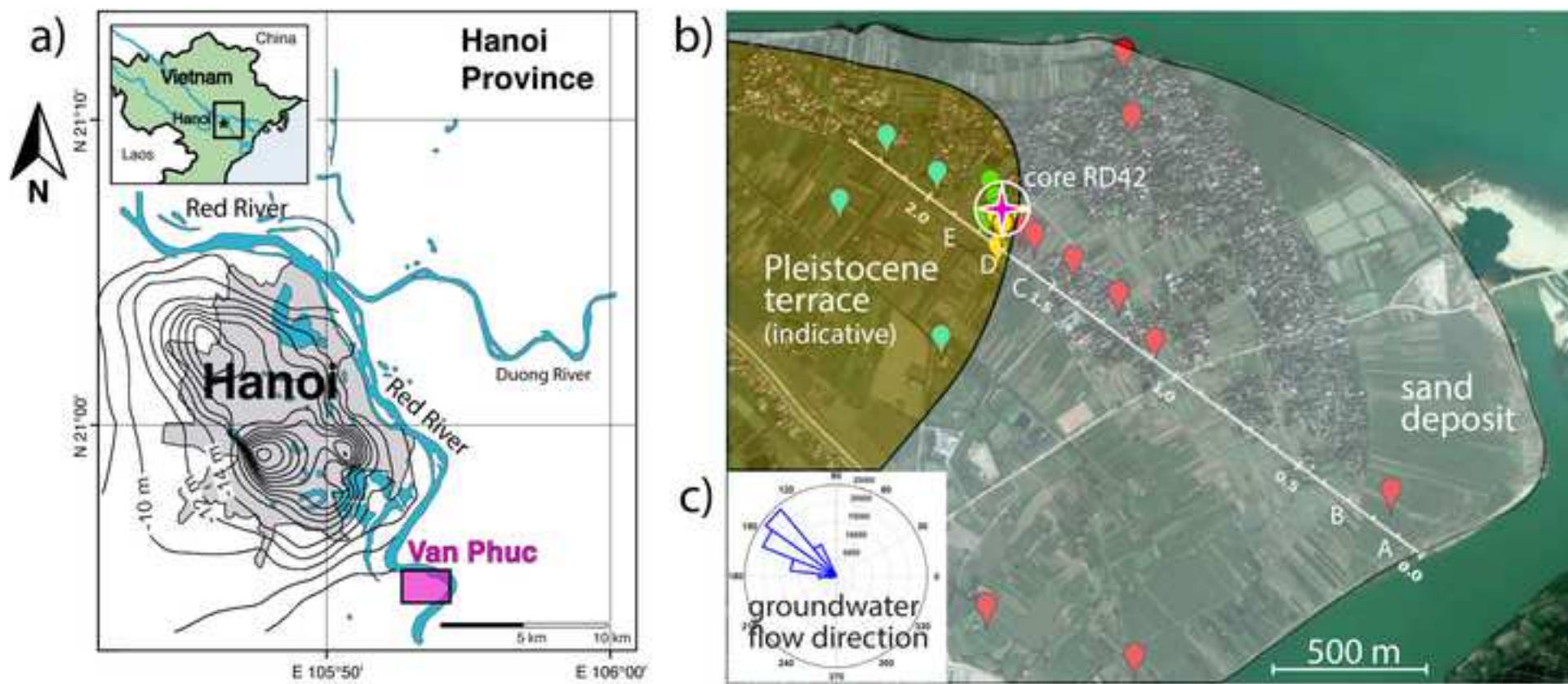


Figure 2

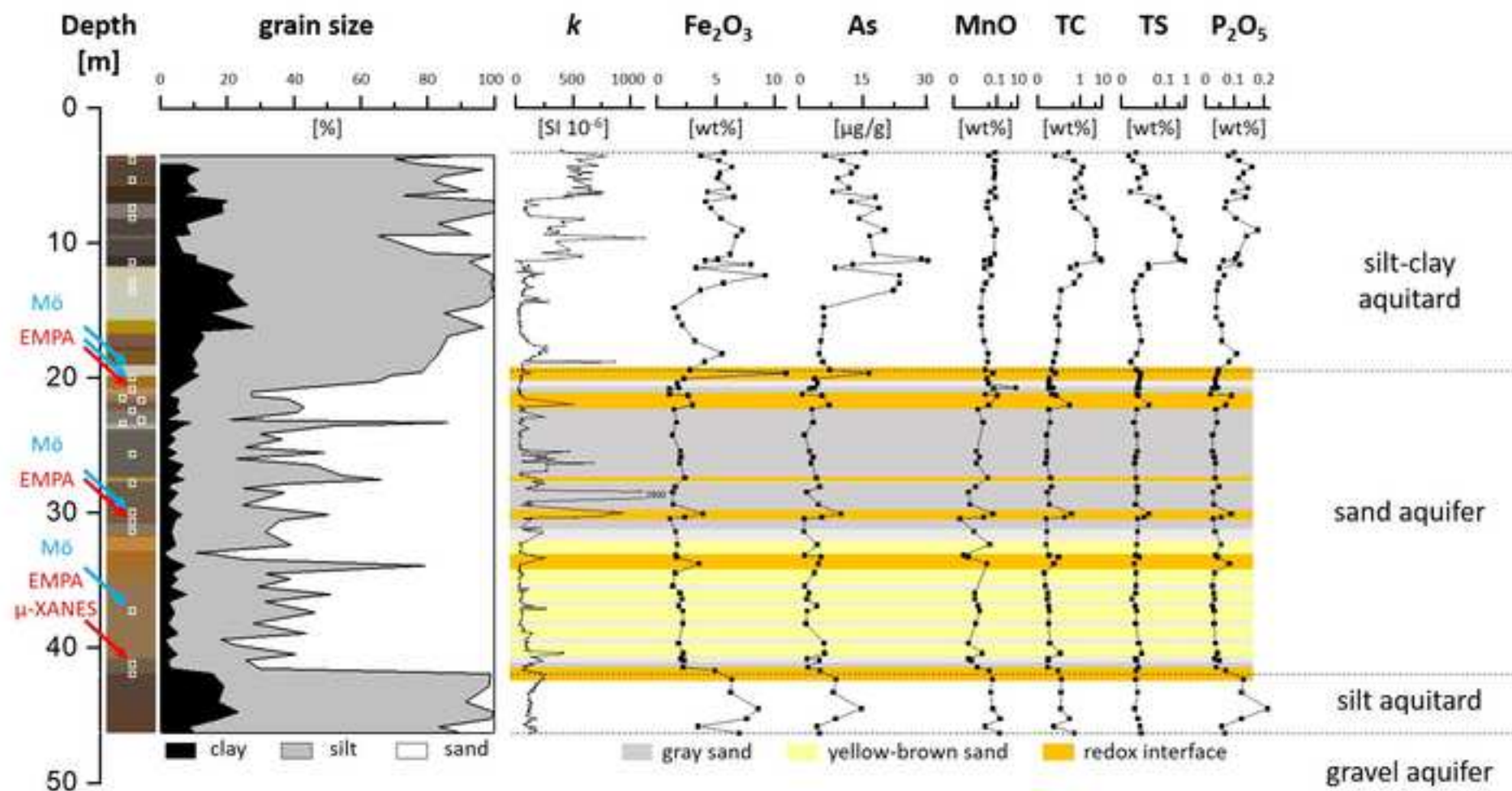


Figure 3

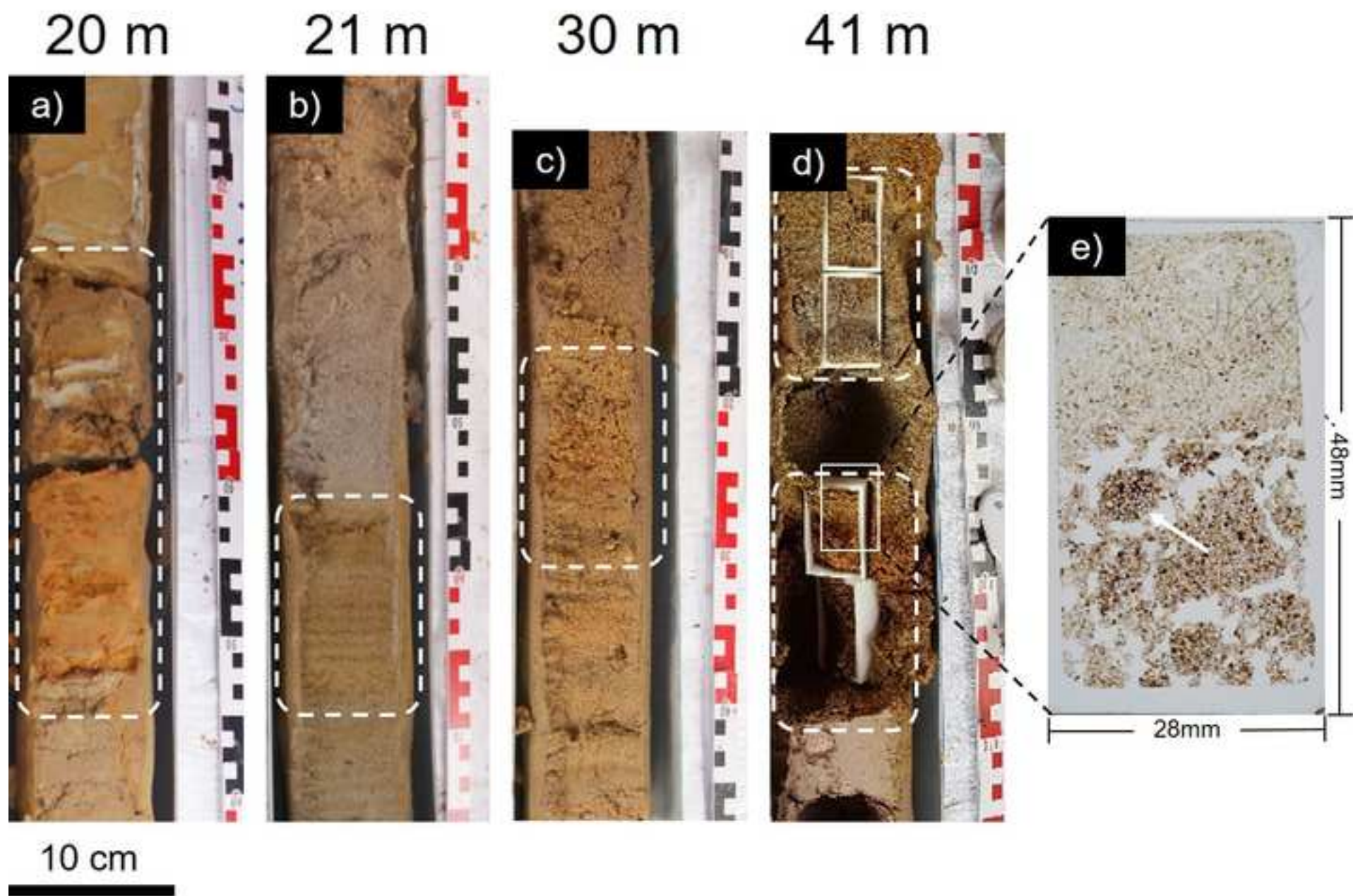


Figure 4

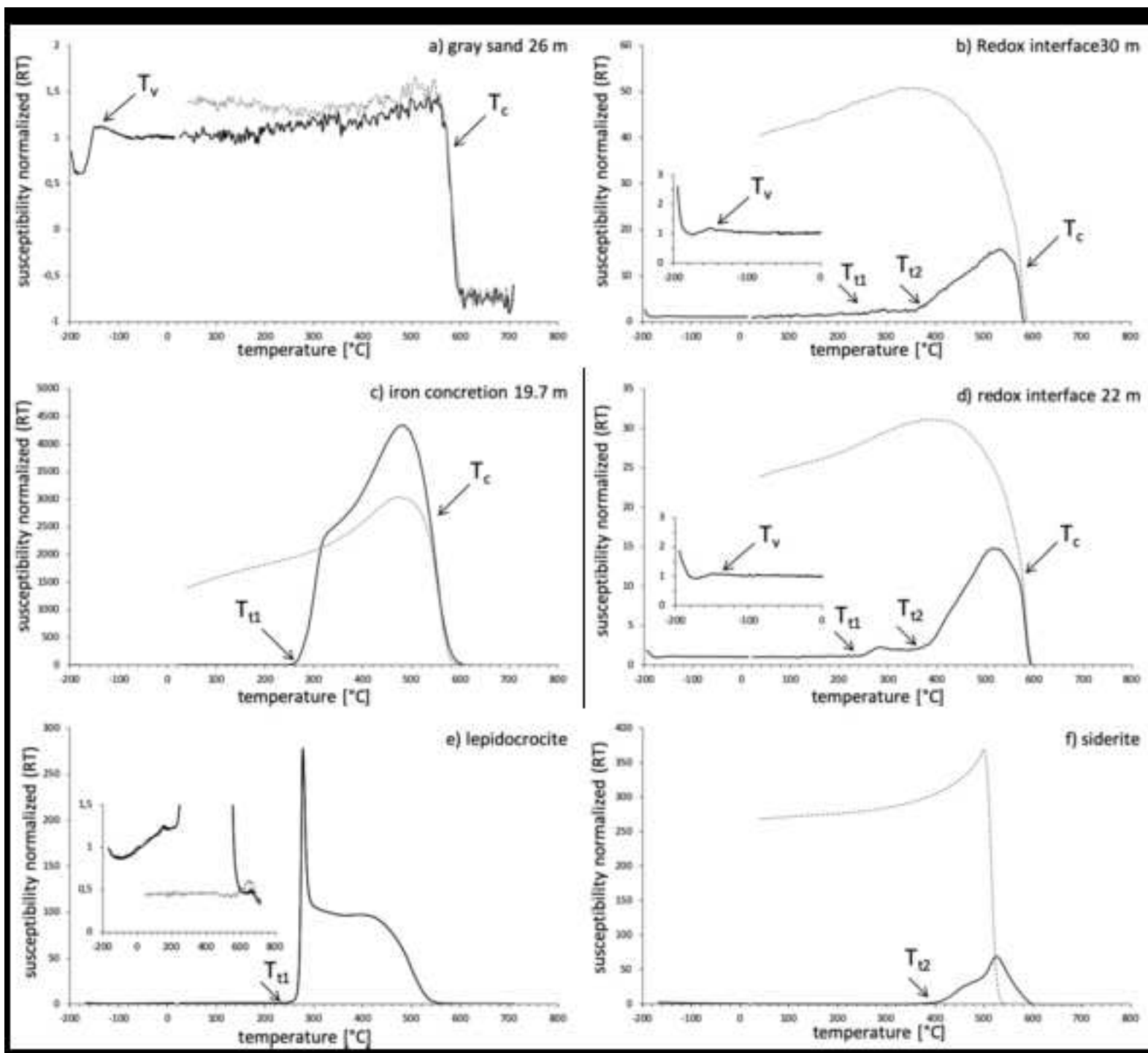


Figure 5

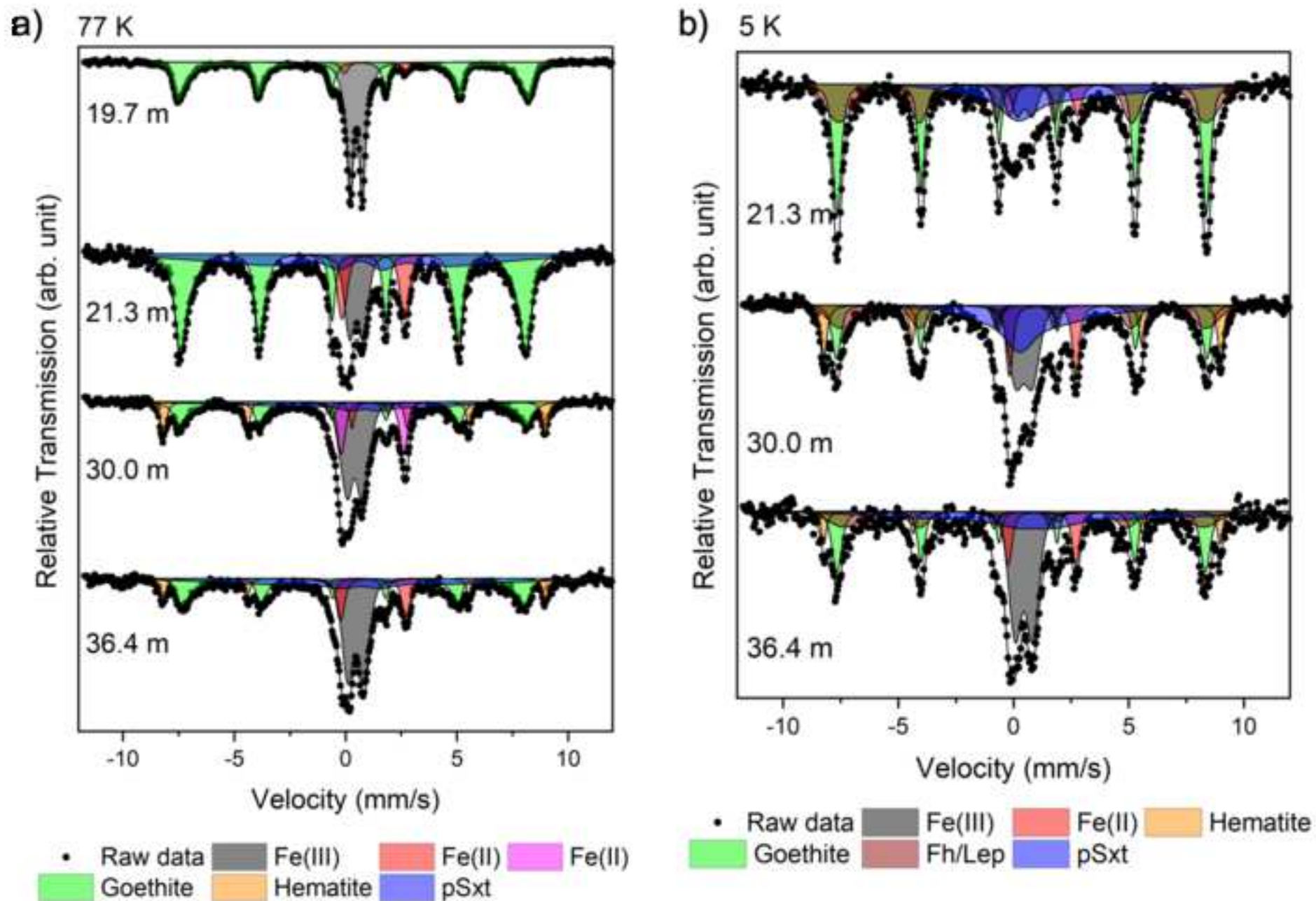


Fig. 6. Scanning electron micrographs of different Fe carbonate

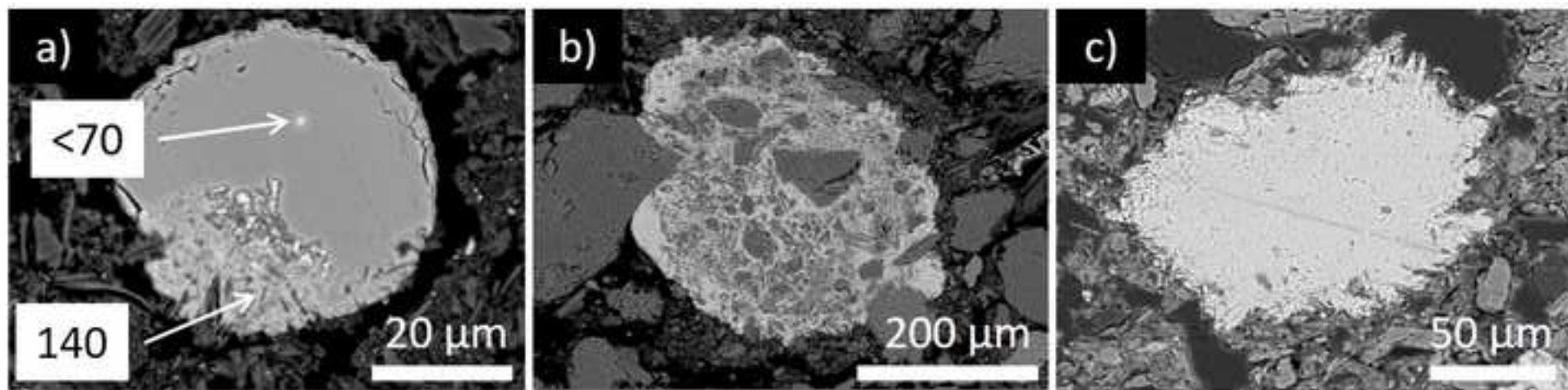


Fig. 7. Scanning electron micrographs of a spherical Fe-rich car

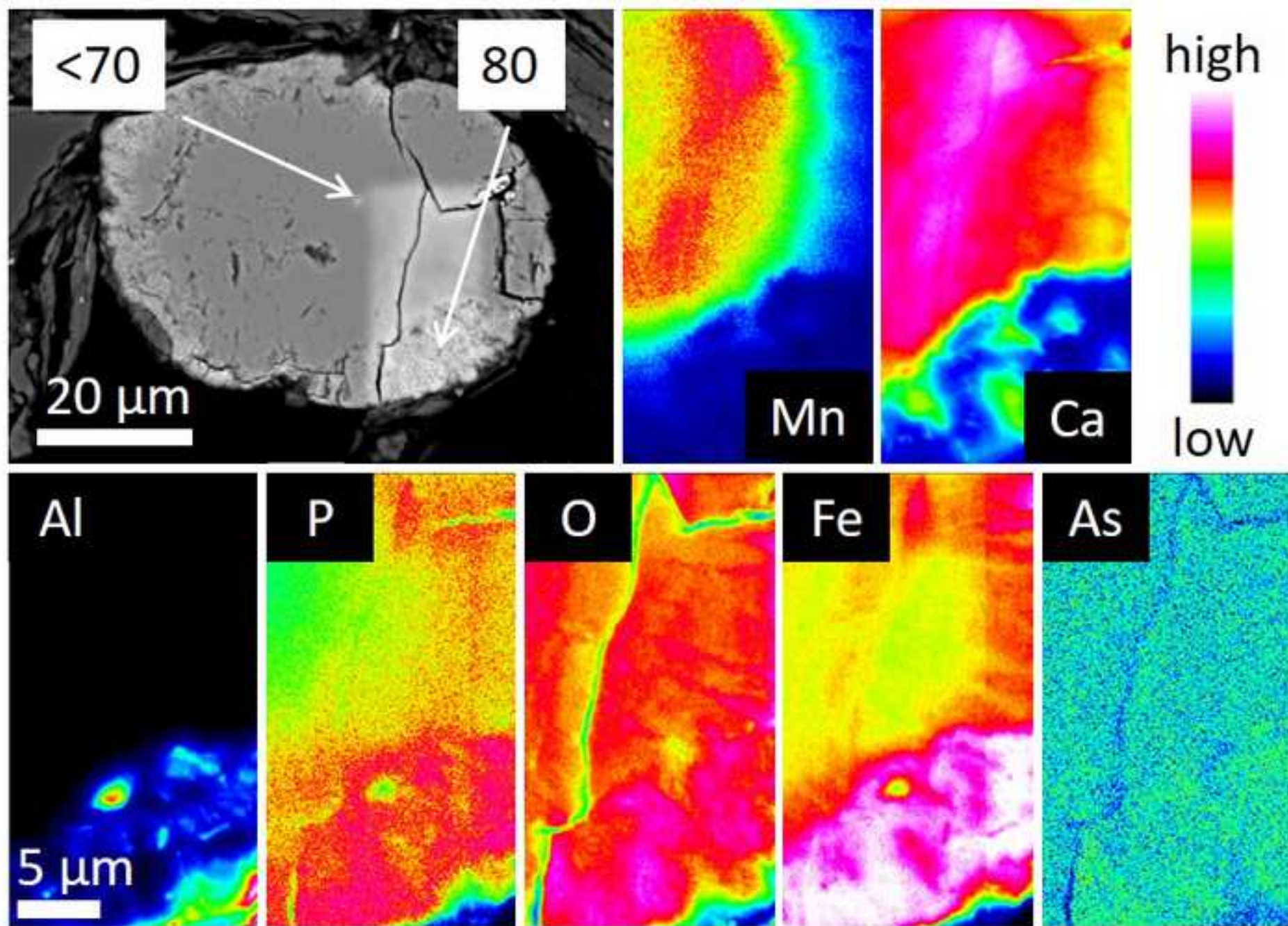


Fig. 8. Scanning electron micrographs of Fe (oxyhydr)oxide preci

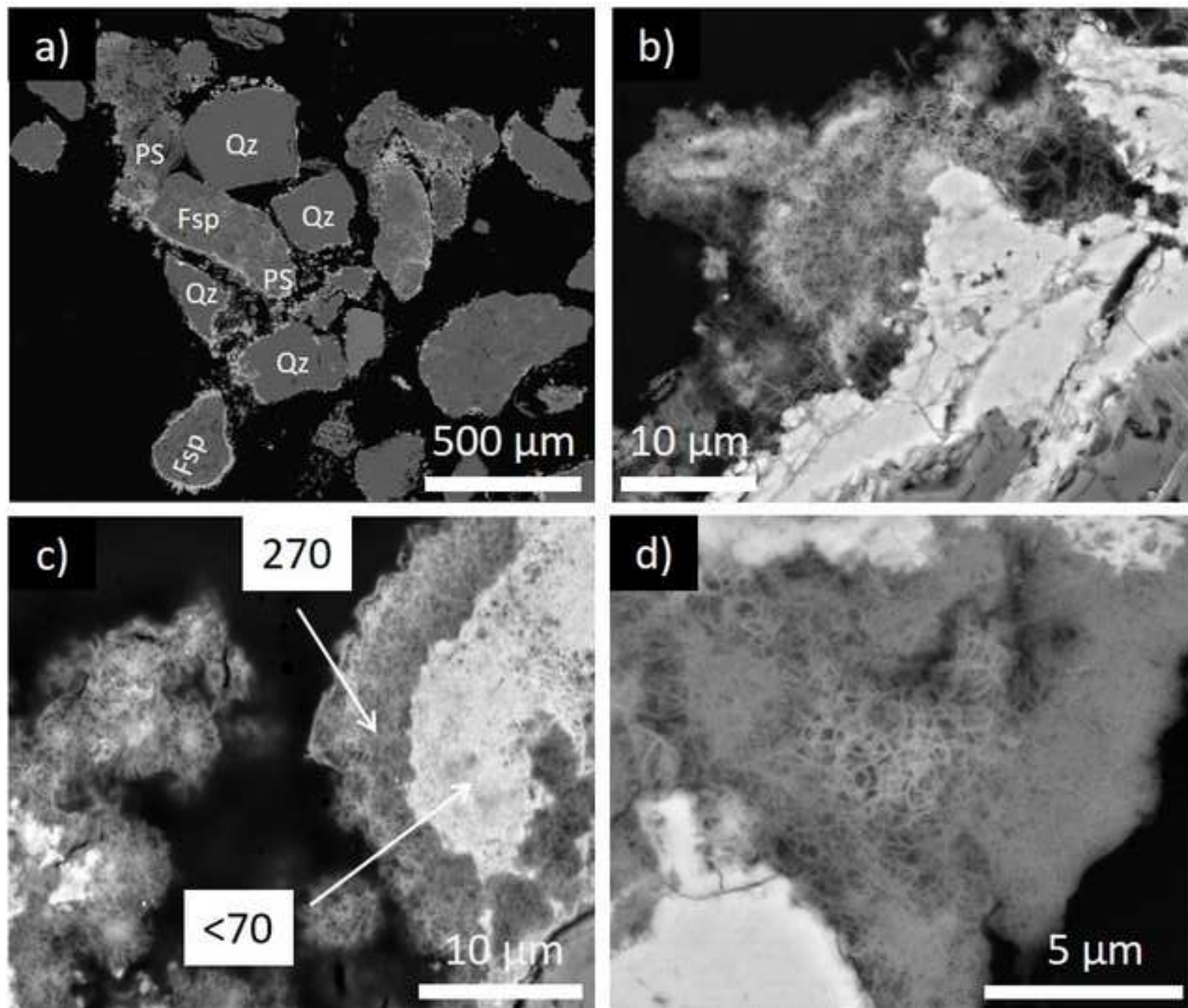


Fig. 9. Scanning electron micrographs of Fe precipitates occurri

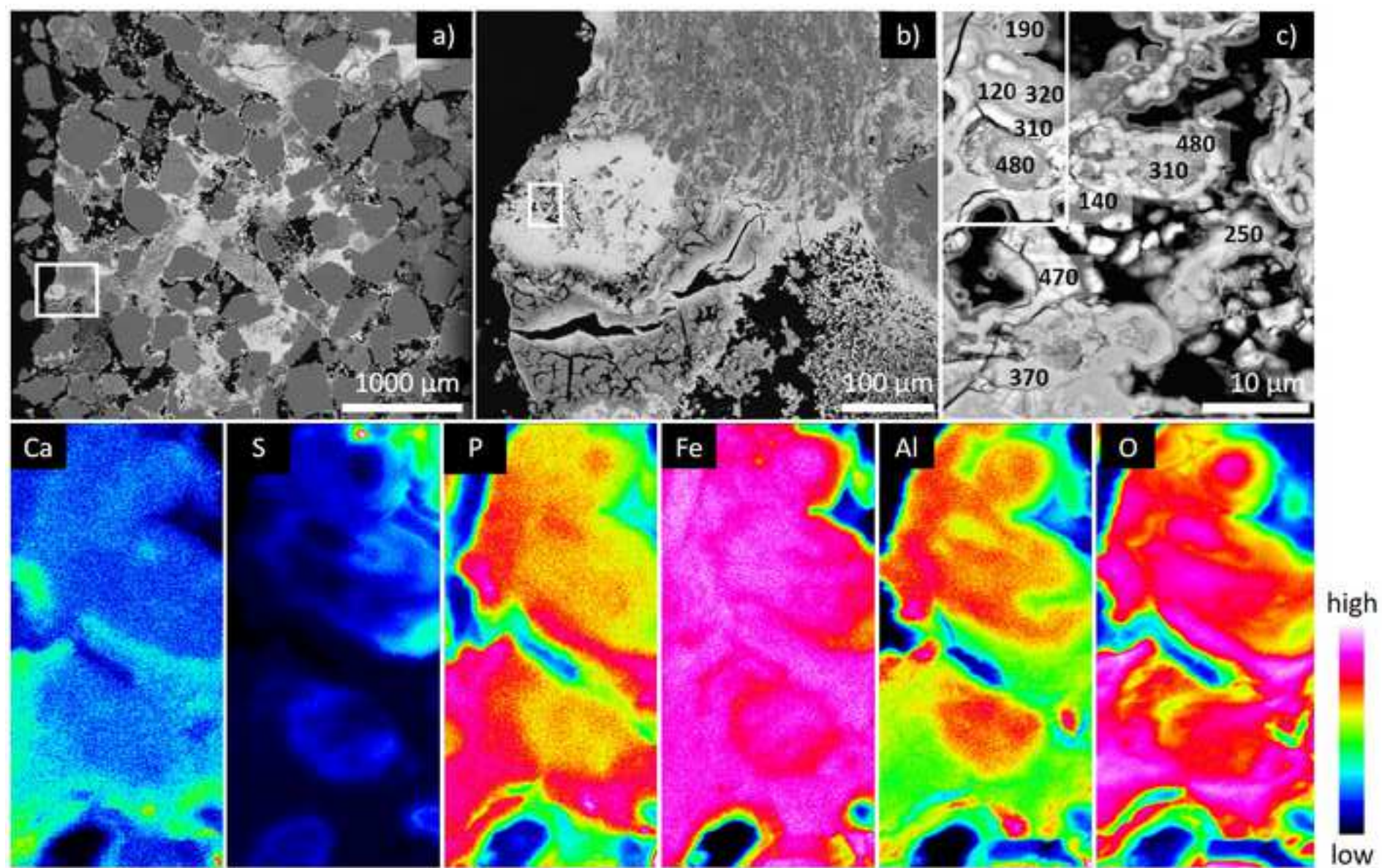


Fig. 10. Photomicrograph of Fe precipitates cementing quartz and

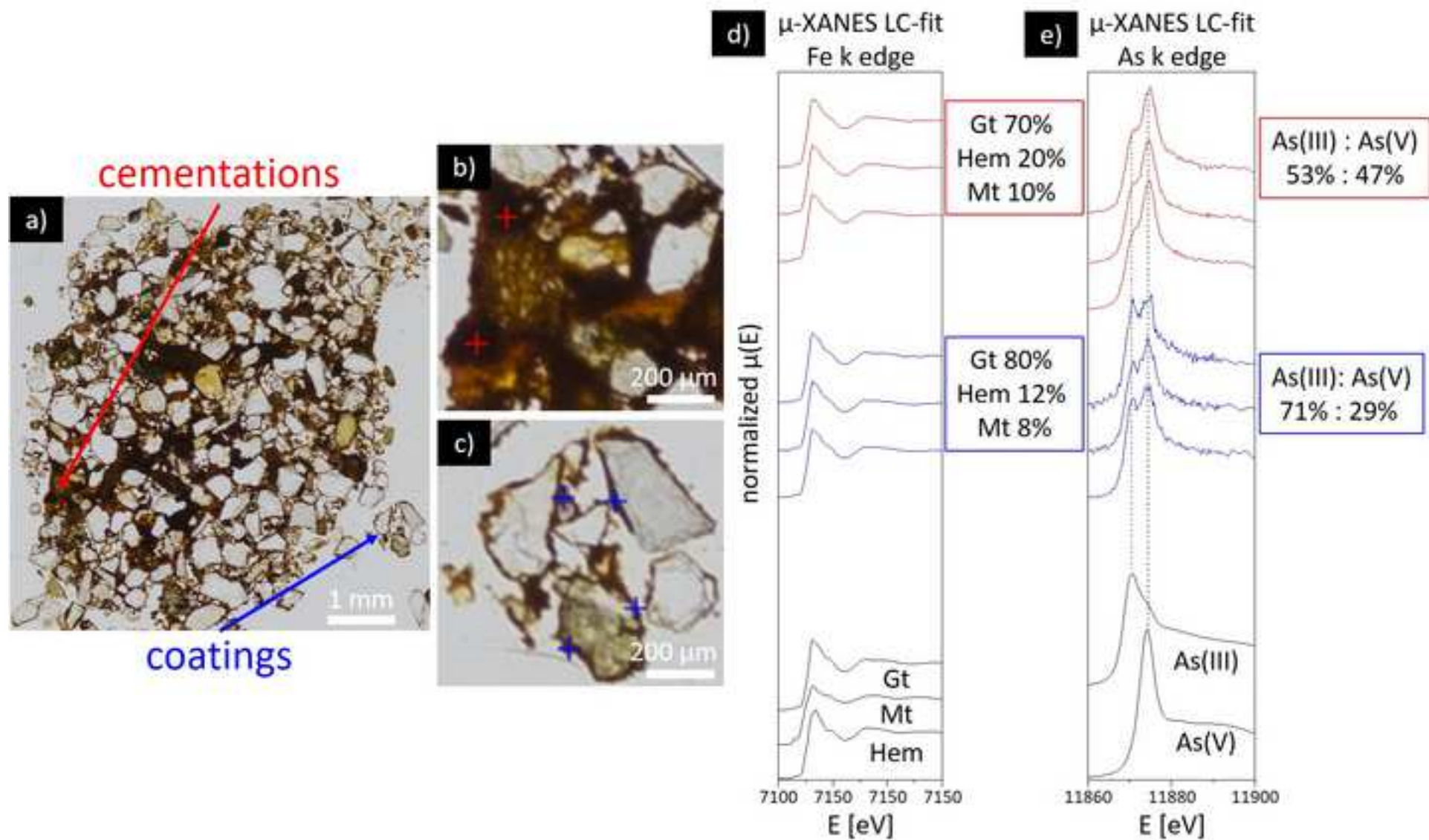


Fig. 11. Scanning electron micrographs of pyrite framboids showi

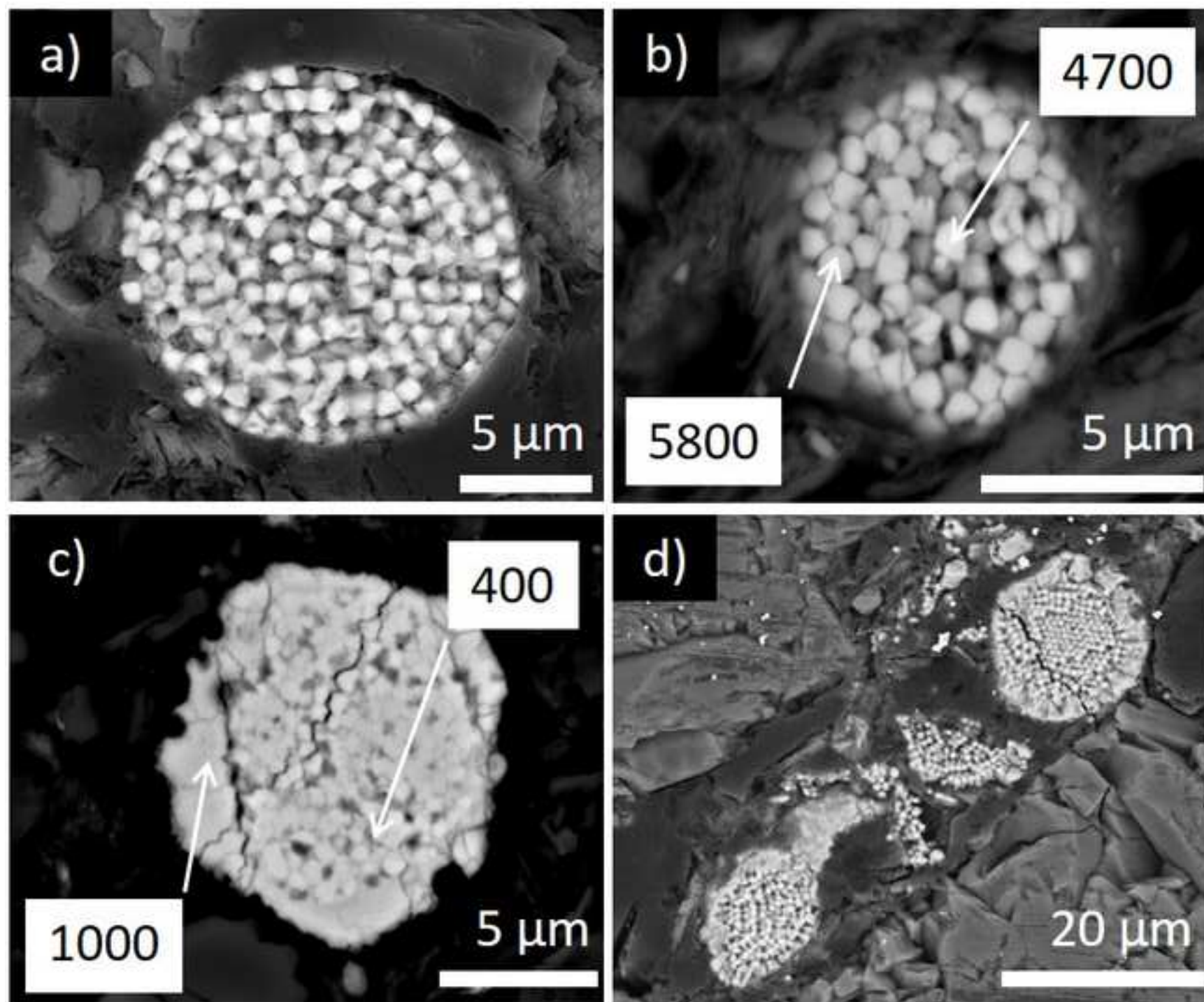


Figure 12

